



# Profiling biomanufactured extracellular vesicles of human forebrain spheroids in a Vertical-Wheel Bioreactor

Chang Liu<sup>1</sup>  | Li Sun<sup>1,2</sup>  | Hannah Worden<sup>3</sup> | Justice Ene<sup>1</sup>  | Olivia Z. Zeng<sup>1</sup> |  
Jamini Bhagu<sup>1,4</sup> | Samuel C. Grant<sup>1,4</sup>  | Xiaoping Bao<sup>5</sup> | Sunghoon Jung<sup>3</sup> | Yan Li<sup>1</sup> 

<sup>1</sup>Department of Chemical and Biomedical Engineering, FAMU-FSU College of Engineering, Florida State University, Tallahassee, Florida, USA

<sup>2</sup>Department of Biomedical Sciences, College of Medicine, Florida State University, Tallahassee, Florida, USA

<sup>3</sup>PBS Biotech Inc, Camarillo, California, USA

<sup>4</sup>National High Magnetic Field Laboratory, Florida State University, Tallahassee, Florida, USA

<sup>5</sup>Davidson School of Chemical Engineering, Purdue University, West Lafayette, Indiana, USA

## Correspondence

Yan Li, Department of Chemical and Biomedical Engineering, FAMU-FSU College of Engineering, Florida State University, 2525 Pottsdamer St., Tallahassee, FL 32310, USA. Email: [yli4@fsu.edu](mailto:yli4@fsu.edu)

Chang Liu, Department of Chemical and Biomedical Engineering, FAMU-FSU College of Engineering, Florida State University, 2525 Pottsdamer St., Tallahassee, FL 32310, USA. Email: [cl20ev@fsu.edu](mailto:cl20ev@fsu.edu)

## Funding information

Division of Chemical, Bioengineering, Environmental, and Transport Systems, Grant/Award Numbers: 1652992, 1917618; National Institute of Neurological Disorders and Stroke, Grant/Award Numbers: R01NS102395, R01NS125016

## Abstract

Extracellular vesicles (EVs) secreted by human brain cells have great potential as cell-free therapies in various diseases, including stroke. However, because of the significant amount of EVs needed in preclinical and clinical trials, EV application is still challenging. Vertical-Wheel Bioreactors (VWBRs) have designed features that allow for scaling up the generation of human forebrain spheroid EVs under low shear stress. In this study, EV secretion by human forebrain spheroids derived from induced pluripotent stem cells as 3D aggregates and on Synthemax II microcarriers in VWBRs were investigated with static aggregate culture as a control. The spheroids were characterized by metabolite and transcriptome analysis. The isolated EVs were characterized by nanoparticle tracking analysis, electron microscopy, and Western blot. The EV cargo was analyzed using proteomics and miRNA sequencing. The in vitro functional assays of an oxygen and glucose-deprived stroke model were conducted. Proof of concept in vivo study was performed, too.

Human forebrain spheroid differentiated on microcarriers showed a higher growth rate than 3D aggregates. Microcarrier culture had lower glucose consumption per million cells and lower glycolysis gene expression but higher EV biogenesis genes. EVs from the three culture conditions showed no differences in size, but the yields from high to low were microcarrier cultures, dynamic aggregates, and static aggregates. The cargo is enriched with proteins (proteomics) and miRNAs (miRNA-seq), promoting axon guidance, reducing apoptosis, scavenging reactive oxygen species, and regulating immune responses. Human forebrain spheroid EVs demonstrated the ability to improve recovery in an in vitro stroke model and in vivo.

Human forebrain spheroid differentiation in VWBR significantly increased the EV yields (up to 240–750 fold) and EV biogenesis compared to static differentiation due to the dynamic microenvironment and metabolism change. The biomanufactured EVs from VWBRs have exosomal characteristics and more therapeutic cargo and are functional in in vitro assays, which paves the way for future in vivo stroke studies.

## KEYWORDS

aggregates, extracellular vesicles, human forebrain spheroids, microcarriers, multi-omics, Vertical-Wheel Bioreactor

This is an open access article under the terms of the [Creative Commons Attribution-NonCommercial-NoDerivs License](https://creativecommons.org/licenses/by-nc-nd/4.0/), which permits use and distribution in any medium, provided the original work is properly cited, the use is non-commercial and no modifications or adaptations are made.

© 2024 The Author(s). *Journal of Extracellular Biology* published by Wiley Periodicals LLC on behalf of International Society for Extracellular Vesicles.

## 1 | INTRODUCTION

Human induced pluripotent stem cells (iPSCs) have been widely investigated recently for in vitro differentiation toward disease modeling, drug screening, and therapeutic applications (Di Lullo & Kriegstein, 2017; Khamis et al., 2023; Zhang et al., 2022). To date, all major brain cell types can be derived from iPSCs, including neural progenitor cells (NPCs), neurons, astrocytes, microglia, oligodendrocytes, vascular endothelial cells, as well as three-dimensional (3D) structures known as brain organoids (Chiaradia & Lancaster, 2020; Penney et al., 2020; Tan et al., 2021). The complexity of brain models can be increased by co-culturing NPCs with other cell types, such as microglia (Park et al., 2023; Song et al., 2019). Besides cell types, brain regional identities can also be patterned such as forebrain and hindbrain (Benito-Kwiecinski & Lancaster, 2020). Maintaining the SMAD pathway inhibition on growing embryoid bodies leads to the generation of aggregates with a high yield of dorsal forebrain identity (Pasca, 2018; Qian et al., 2016).

The traditional method of generating spheroids or organoids is via static ultra-low attachment plates (Choi et al., 2022; Ko et al., 2021; Song et al., 2019). The formed 3D structure in a static condition faces challenges such as diffusion limitation of nutrients and oxygen and the need for removal of metabolic waste (Choi et al., 2022). To enhance the diffusion efficiency, dynamic 3D culture conditions, such as bioreactors, were proposed. The commonly used bioreactors are spinner flasks and rotating wall bioreactors (Huang et al., 2022; Liu et al., 2021). The spinner flask has limited capacity for iPSC culture either as spheroids or attached to microcarriers in suspension, due to the necessity of high agitation speeds which may generate high shear rates and hamper cell growth (de Sousa Pinto et al., 2019). In a rotating wall bioreactor setup, the culture vessel is rotated around a horizontal axis and has low shear stress. However, its scale-up is challenging, limiting its capacity to produce enough cells for clinical applications (Kumar & Starly, 2015).

Recently, Vertical-Wheel Bioreactor (VWBR) was designed for human stem cell culture, which has a U-shaped bottom with a vertically rotating wheel (Sousa et al., 2015). The impeller itself accounts for ~85% of the width of the U-shaped bottom, and it creates a combination of radial and axial flow. The radial component comes from the vertical rotation of the impeller, and the axial component comes from the vanes in the impeller. The vanes are positioned to generate flow in opposite directions (Sousa et al., 2015). These designs allow for efficient mixing at very low shear rates, about 10-fold lower compared to traditional stirred tank bioreactors (0.1–0.3 dyn/cm<sup>2</sup> vs. 1–3 dyn/cm<sup>2</sup> respectively), and are applicable for scale-up to 500 L (Dang et al., 2021; Sousa et al., 2015). VWBR has been reported for human mesenchymal stem cells (MSCs) grown on microcarriers (de Sousa Pinto et al., 2019; Jeske et al., 2023; Lembong et al., 2020; Sousa et al., 2015), and expansion of human iPSCs as aggregates (Borys et al., 2020, 2021; Nogueira et al., 2019) or grown on microcarriers (Rodrigues et al., 2018). The hydrodynamic microenvironment was proven to enhance stem cell production and reduce manufacturing costs. Moreover, VWBR was employed for iPSC-derived pancreatic islets and cerebellar organoid differentiation (Dadheech et al., 2023; Silva et al., 2021), showing faster lineage-specific commitment with clinical-grade quality.

Extracellular vesicles (EVs) are a group of small, lipid-bound nanoparticles that can be secreted by any type of cell (van Niel et al., 2018; Yuan et al., 2022). They carry a variety of cargo, including DNAs, microRNAs, proteins, and lipids, playing key roles in cell-cell communications (Cheng & Hill, 2022; Raposo & Stahl, 2019; van Niel et al., 2022). Their homing ability results in specific tissue localization, which contributes to their therapeutic potential. For example, choroid plexus epithelial cell-derived EVs homed to the choroid plexus in mouse brain and functionally delivered cargo to astrocytes and microglia (Pauwels et al., 2022). NPC-derived EVs demonstrated the ability to significantly reduce cell injury and enhance neurological recovery after stroke both in vitro and in vivo (Tian et al., 2021; Zheng et al., 2021). EVs from human forebrain organoids were isolated in our previous study, and shown to be feasible for superparamagnetic iron oxide labeling and magnetic resonance imaging, but no EV cargo analysis or functional evaluations were performed (Liu et al., 2022). For clinical treatments of brain disorders, the demand for EVs from brain-related cells is huge. For instance, in a summary of 50 different preclinical animal studies, the median EV dose based on protein amount was 2.75 mg EV protein per kg body weight per dose (Gupta et al., 2021), and one million cells only generated several micrograms of EV protein (Gudbergsson et al., 2016). Thus, a human body would require a trillion cells to harvest EVs that are sufficient for just one dose. In recent years, a few studies have been using VWBR for EV production mainly from MSCs (de Almeida Fuzeta et al., 2020; Jalilian et al., 2022; Jeske et al., 2023; Otahal et al., 2023). However, the EV generation and composition from iPSC-derived cells in VWBRs have not been well investigated.

In our previous studies (Arthur et al., 2023; Muok et al., 2024), EV biogenesis of undifferentiated human iPSCs was promoted in VWBR and the EV composition was found to be affected by 3D culture organization. In this study, human iPSCs were differentiated toward forebrain spheroids in VWBR, which grew as aggregates/spheroids or microcarriers. The static aggregate/spheroid culture served as a control. Spheroids were characterized in terms of growth kinetics, metabolites, transcriptome signature, gene expression, and neural differentiation potential. EVs were isolated from spent culture media and were characterized for size, yield, purity, and exosome markers, in particular, the protein and miRNA cargo profiles based on multi-omics. Besides, EVs were evaluated in an in vitro stroke model to regulate metabolic activity, apoptosis, and oxidative stress as functional analysis. Previous literature only reported the EV composition of iPSC-derived neural stem cells from 2D differentiation (Huang et al., 2020). To our knowledge, this is the first study about a systematic and comprehensive analysis of proteome and miRNA profiles

of EVs secreted by 3D human forebrain spheroids in a dynamic VWBR. This study advances our understanding of a scalable biomanufacturing system for EV generation from forebrain spheroids as cell-free therapeutics (Abdollahi, 2021). In particular, the effects of hydrodynamics and 3D organization on EV composition were revealed toward the application to ischemic stroke therapy.

## 2 | MATERIALS AND METHODS

### 2.1 | Undifferentiated human iPSC culture

Human iPSCs (Pluristyx) were thawed from the vial of the Matched Research Grade human iPSC Working Cell Bank (WCB) generated under current good manufacturing practice (cGMP) from Lonza (Walkersville, MD, USA). Human iPSCs were reprogrammed from human CD34+ umbilical cord blood cells using a non-integrating episomal vector reprogramming method (Certificate of Analysis and Lutheran Hospital Institutional Review Board Approval available upon request). Human iPSCs cryogenically preserved in CryoStor CS10 (StemCell Technologies Inc., Vancouver, Canada) were thawed and plated into growth factor reduced Matrigel (BD Biosciences, Franklin Lakes, NJ, USA)-coated CellBIND T-25 cm<sup>2</sup> and T-75 cm<sup>2</sup> Rectangular Canted Neck Cell Culture Flasks with Vent Cap (Corning Inc., Corning, NY, USA). Cells were seeded at a density of 15,000 cells/cm<sup>2</sup> and grown for 3 days as P+1 and 5000 cells/cm<sup>2</sup> for 4 days as P+2 in mTeSR media (StemCell Technologies Inc.) in a standard incubator (5% CO<sub>2</sub>, 37°C) with daily media feeding. Cells were passaged with Accutase (StemCell Technologies Inc.) twice and then harvested for VWBR inoculation.

### 2.2 | Aggregate and microcarrier-based forebrain cortical differentiation in VWBRs

The experimental plan and design are shown in Figure 1. Human iPSCs were cultured for two passages before seeding in bioreactors for differentiation (Figure 1a). There were three culture conditions: (1) aggregates formed in the VWBR without microcarriers (Agg), (2) cells attached to microcarriers and grew in VWBR (MC), and (3) aggregates formed in static ultralow attachment 6-well plates without microcarriers (6-well). Each culture condition had two seeding densities:  $2 \times 10^4$  cells/mL (L for low density) and  $1 \times 10^5$  cells/mL (H for high density). All the cells were differentiated for 12 days with supplements shown in Figure 1b. From D0 to D1, the cells were maintained in mTeSR. After D1, cells were cultured in DMEM/F12 plus B27 with medium change every 2 days. At D12, the cells were harvested for evaluating growth and differentiation, and the media were collected for EV isolation (Figure 1c).

#### 2.2.1 | Aggregate-based differentiation (forebrain spheroids)

For the aggregates in a bioreactor, the vessels were filled up to 100 mL medium and were maintained at 40 rpm. For the aggregates in ultra-low attachment 6-well plates (Corning Inc.), each well was filled with 3 mL media. Cells equivalent to microcarrier-based bioreactors (L:  $2 \times 10^4$  cells/mL or H:  $1 \times 10^5$  cells/mL) were seeded. The feeding timeline was the same as microcarrier-based differentiation. Three independent runs were performed for microcarrier and aggregate conditions.

#### 2.2.2 | Microcarrier-based differentiation

Corning Synthemax II Microcarriers (360 cm<sup>2</sup>/gram, Corning Inc.) were added to the VWBRs (PBS Biotech Inc., Camarillo, CA, USA) (Yuan et al., 2022) at a concentration of 20 g/L. For 100 mL (0.1 L), 2 grams were used and the total surface area was 720 cm<sup>2</sup>. The bioreactors were inoculated with two seeding densities, L:  $2 \times 10^4$  or H:  $1 \times 10^5$  cells/mL, corresponding to  $2.8 \times 10^3$  or  $1.4 \times 10^4$  cells/cm<sup>2</sup>, respectively. The vessels were filled up to the seeding volume with mTeSR media (60 mL for the 0.1 L vessels). Vessels were then maintained at 40 rpm for 24 h for cell attachment. On day one, 70% of the media were exchanged to DMEM/F12 (Gibco Inc., Billings, MT, USA) containing B27 (Gibco Inc.). Media exchange was performed on D3, D6, D8, and D10, and the cells were harvested on D12. On D1, D3, and D6, small molecules SB 431542 (Sigma-Aldrich, St. Louis, MO, USA) and LDN 193189 (Sigma-Aldrich) were added into the media; and on D8, D10, fibroblast growth factor 2 (FGF2, PeproTech, Inc., Cranbury, NJ, USA) were added (Figure 1a).

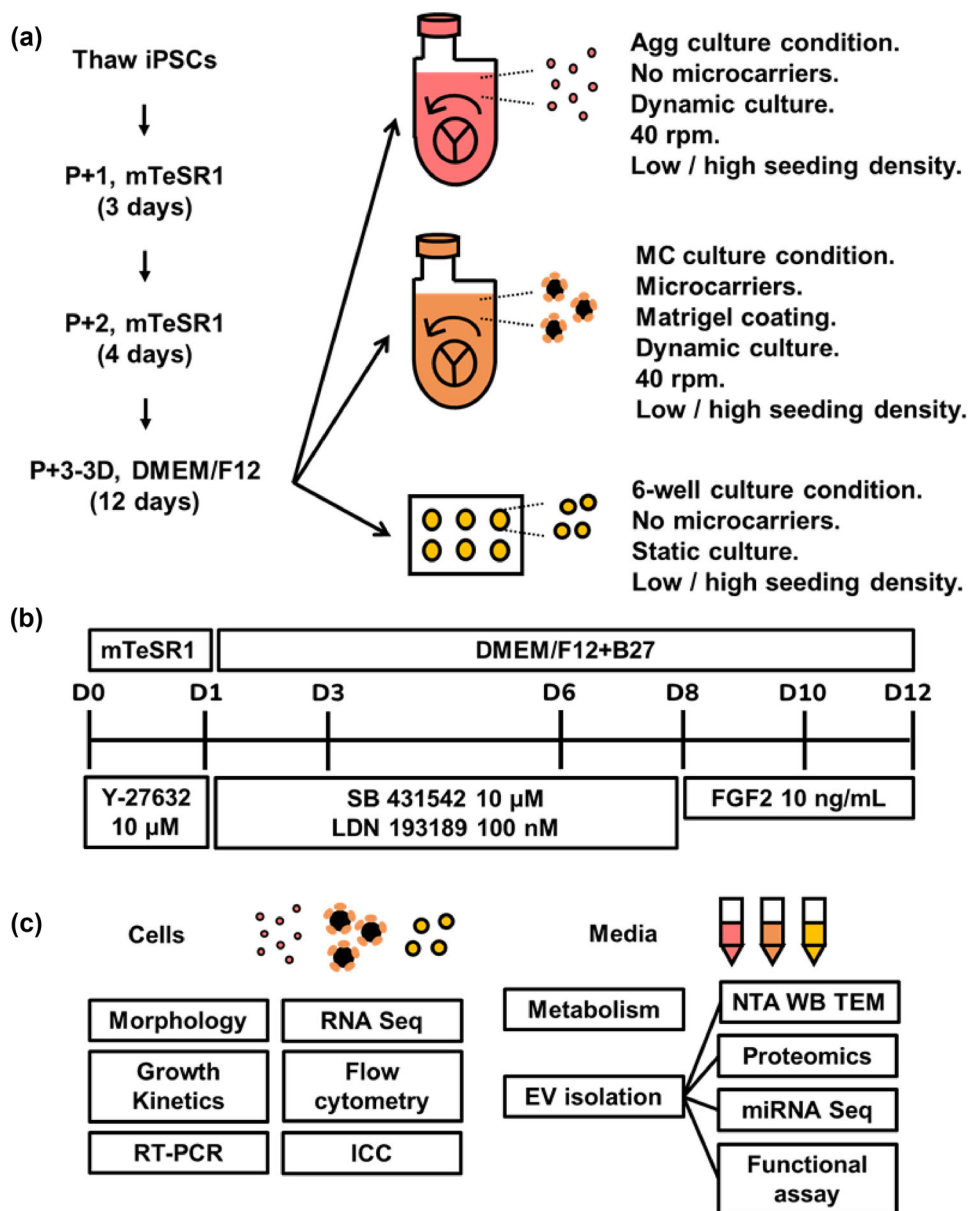


**FIGURE 1** Schematics of (a) Human iPSC seeding plan, (b) differentiation timeline, and (c) experimental design. Agg, aggregates grown in the VWBR; MC, cells attached to Matrigel-coated microcarriers in the VWBR; 6-well, aggregates grown as static culture in 6-well plates.

### 2.3 | Cell number and metabolite measurements

For sampling of each bioreactor, 3 mL of samples were taken out for cell count and metabolite analysis on days 3, 6, 8, 10, and 12. One millilitre of samples was removed for microscopic observation. For cell counts, the cells were spun at 500 g for 5 min. The supernatant was then removed and frozen for metabolite analysis. The spent media were analyzed with a BioProfile Flex2 (Nova Biomedical, Waltham, MA, USA) analyzer for metabolite concentration. The cells were re-suspended and dissociated in Accutase. The cell suspension was loaded into a Vial-Cassette (ChemoMetec, Bohemia, NY, USA), which was subsequently loaded into a NucleoCounter NC-200 (ChemoMetec, Bohemia, NY, USA) that determined cell concentration. Each measurement was performed with three replicates.

### 2.4 | Cell harvest, media collection, and EV isolation

For bioreactors, microcarriers and aggregates in the media were collected while maintaining 48 rpm agitation. The conditioned media were centrifuged at 500 g for 5 min and the supernatants were stored at  $-80^{\circ}\text{C}$  for EV isolation. The cells were dissociated

by Accutase, resuspended in FreSR-S cryopreservation medium (StemCell Technologies Inc.), and then stored at  $-80^{\circ}\text{C}$  for further analysis. To isolate EVs, the modified differential ultracentrifugation method was performed. Briefly, the conditioned media were centrifuged at 500 g for 5 min. The supernatants were collected and centrifuged again at 2000 g for 10 min. The collected supernatants were then centrifuged at 10,000 g for 30 min. EVs were isolated using an inexpensive polyethylene glycol (PEG)-based method as reported previously (Marzano et al., 2019, 2021; Rider et al., 2016). After centrifugation at 10,000 g for 30 min, supernatants were collected and mixed with PEG solution (24% wt/vol in 1.5 M NaCl) at a 2:1 volume and incubated at  $4^{\circ}\text{C}$  overnight. The mixed solutions were centrifuged at 3000 g for 1 h. The crude EV pellets were resuspended in filtered PBS and then ultra-centrifuged at 100,000 g for 70 min. Purified EV pellets were resuspended in 100  $\mu\text{L}$  PBS and stored in freezer for further use.

## 2.5 | Nanoparticle tracking analysis (NTA)

NTA was performed on the isolated EV samples in triplicate to determine size distribution and particle concentration on a Nanosight LM10-HS instrument (Malvern Instruments, Malvern, UK) configured with a blue (488 nm) laser and sCMOS camera (Rider et al., 2016). For each replicate, three videos of 60 s were acquired with camera shutter speed fixed at 30.00 ms. To ensure accurate and consistent detection of small particles, the camera level was set to 13, and the detection threshold was maintained at 5. The laser chamber was cleaned thoroughly with particle-free water between each sample reading. The collected videos were analyzed using NTA3.4 software to obtain the mode and mean size distribution, as well as the concentration of particles per mL of solution. Compared to the mean size, the mode size is usually a more accurate representation because the vesicle aggregates may affect the value of the mean size.

## 2.6 | Transmission electron microscopy (TEM)

TEM was performed to confirm the morphology of EVs as shown in our previous publication (Marzano et al., 2019). Briefly, EV isolates were resuspended in 50–100  $\mu\text{L}$  of sterile filtered PBS. For each sample preparation, intact EVs (15  $\mu\text{L}$ ) were dropped onto Parafilm. A carbon-coated 400 Hex Mesh Copper grid (Electron Microscopy Sciences, EMS) was positioned using forceps with the coating side down on top of each drop for 1 h. Grids were washed with sterile filtered PBS three times, and then the EV samples were fixed for 10 min in 2% PFA (EMS, EM Grade). After washing, the grids were transferred on top of a 20  $\mu\text{L}$  drop of 2.5% glutaraldehyde (EMS, EM Grade) and incubated for 10 min at room temperature. Grid samples were stained for 10 min with 2% uranyl acetate (EMS grade). Then the samples were embedded for 10 min with 0.13% methylcellulose and 0.4% uranyl acetate. The coated side of the grids was left to dry before imaging on the Transmission Electron Microscope HT7800 (Hitachi, Japan).

## 2.7 | Western blotting for EV markers

EV and cell samples were lysed in radio-immunoprecipitation assay (RIPA) buffer (150 mM sodium chloride, 1.0% Triton X-100, 0.5% sodium deoxycholate, 0.1% sodium dodecyl sulfate, 50 mM Tris, pH 8.0 and Halt Protease Inhibitor Cocktail (Thermo Fisher Scientific Inc., Waltham, MA, USA)). Samples were incubated for 20 min on ice, and spun down at  $4^{\circ}\text{C}$  14,000 g for 20 min. The supernatant was collected, and a Bradford assay was carried out to determine the protein concentration. Protein lysate concentration was normalized, and denatured at  $90$ – $100^{\circ}\text{C}$  in 2 X Laemmli Sample buffer for 5 min. About 15–20  $\mu\text{g}$  of proteins were loaded into each well. Proteins were separated by 12% Bis-Tris-SDS gels and transferred onto a nitrocellulose membrane (Bio-Rad, Hercules, CA, USA). The membranes were blocked for 1 h in 5% skim milk (w/v) in Tris-buffered saline (10 mM Tris-HCl, pH 7.5, and 150 mM NaCl) with 0.1% Tween 20 (v/v) (TBST). Membranes were incubated overnight in the presence of the primary antibodies (Table S1) diluted in blocking buffer at  $4^{\circ}\text{C}$ . Afterward, the membranes were washed four times with TBST and then incubated with an IR secondary (LI-COR, Lincoln, NE) at 1:5000 for 90 min at room temperature. Blots were washed four more times with TBST and processed using the LI-COR Odyssey (LI-COR).

## 2.8 | Immunocytochemistry and flow cytometry

For biomarker detection, the cells were fixed using 4% paraformaldehyde (PFA) and permeabilized using 0.2% Triton-X 100. The samples were blocked with 5% FBS in PBS and stained with the primary antibodies (Table S1), followed by Alexa Fluor 488 goat anti-mouse IgG1 or Alexa Fluor 594 goat anti-Rabbit IgG (Life technologies). Both primary and secondary antibodies were diluted in staining buffer (2% FBS in PBS) based on the manufacturer's recommendations. Then, the nuclei were counterstained with

Hoechst 33342, and images were taken under a fluorescent microscope (Olympus IX70, Melville, NY). For marker quantification, the flow cytometry method was used. Briefly,  $1 \times 10^6$  cells were fixed with 4% PFA and washed with staining buffer (2% FBS in PBS). The cells were permeabilized with 100% cold methanol, blocked with blocking buffer (5% FBS in PBS), and then incubated with different primary antibodies (Table S1) followed by the corresponding secondary antibody. The cells were acquired using BD FACSCanto II flow cytometer (Becton Dickinson) and analyzed against isotype controls using FlowJo software (v10).

## 2.9 | Reverse transcription and quantitative polymerase chain reaction (RT-qPCR)

Total RNA was isolated from different cell samples using the RNeasy Mini Kit (Qiagen, Valencia, CA) according to the manufacturer's protocol. The isolated RNA samples were further treated with a RNase-Free DNase Kit (Zymo, Irvine, CA, USA) to remove genomic DNA contamination (Song et al., 2016). Reverse transcription was carried out according to the manufacturer's instructions using 2  $\mu$ g of total RNA, anchored oligo-dT primers (Operon, Huntsville, AL), and Superscript III (Invitrogen, Carlsbad, CA, USA). The software Oligo Explorer 1.2Primers (Genelink, Hawthorne, NY, USA) was used to design the real-time PCR primers specific for target genes (Table S2). For normalization of expression levels,  $\beta$ -actin was used as an endogenous control. Using SYBR1 Green PCR Master Mix (Applied Biosystems, Foster City, CA, USA), real-time PCR reactions were performed on an ABI7500 instrument (Applied Biosystems). The amplification reactions were performed as follows: 10 min at 95°C, and 40 cycles of 95°C for 15 s, 55°C for 30 s, and 68°C for 30 s following with a melt curve analysis. The Ct values of the target genes were first normalized to the Ct values of the endogenous control  $\beta$ -actin. The corrected Ct values were then compared for the bioreactor conditions to the static control. Fold changes in gene expression were calculated using the comparative Ct method:  $2^{-(\Delta C_{t \text{ treatment}} - \Delta C_{t \text{ control}})}$  to obtain the relative expression levels.

## 2.10 | Liquid chromatography-tandem mass spectrometry (LC-MS/MS) based proteomics analysis of EV protein cargo

The EVs (from the high seeding density cultures) were isolated using ExtraPEG and then extracted for proteins. Based on protein quantification results, up to 24  $\mu$ g proteins were isolated on the S-trap micro column (Protifi). The isolated proteins were alkylated and digested on a column based on the manufacturer's instructions. Then, all the samples (triplicate for each group) were vacuumed dried and submitted to Florida State University Translational Science Laboratory. The samples were analyzed on the Thermo Q Exactive HF as previously described (Hurwitz & Meckes, 2017; Hurwitz et al., 2018). Briefly, the resulting raw files were searched with Proteome Discoverer 2.4 using SequestHT, Mascot and Amanda as search engines. Scaffold (version 5.0) was used to validate the protein and peptide identity. Peptide identity was accepted if Scaffold Local false discovery rate (FDR) algorithm demonstrated a probability greater than 99.0%. Likewise, protein identity was accepted if the probability level was greater than 99.0% and contained a minimum of two recognized peptides. Gene Ontology (GO) annotation was carried out by g:Profiler.

## 2.11 | mRNA sequencing for differentiated forebrain spheroids transcriptome analysis

Total RNA from differentiated forebrain spheroids were isolated by Trizol reagent (ThermoFisher) and were further treated with a DNA-Free RNA Kit to remove genomic DNA contamination. Then, the mRNA-seq library was prepared by a combination of NEBNext Ultra RNA Library Prep Kit (NEB) and NEBNext Poly(A) mRNA Magnetic Isolation Module (NEB). The constructed libraries were run on Bioanalyzer with HS DNA chip (Agilent) for quality control and finally quantified by KAPA library quantification kit (KAPA). Then, the libraries were pooled at equal molar amounts and submitted to the Florida State University College of Medicine Translational laboratory for sequencing on Illumina NovaSeq 6000 system.

## 2.12 | Small RNA sequencing for EV miRNA cargo analysis

EV-associated miRs were isolated and sequenced in triplicate. EV samples were treated with RNase (ThermoFisher) to a final concentration of 50 ng/mL, at room temperature for 30 min. RNase inhibitor (NEB) and PCR-grade water were added to EV samples to make a total volume of 200  $\mu$ L. miRs were isolated by adding 600  $\mu$ L Trizol LS (ThermoFisher) according to the manufacturer's instruction. To increase the yield of small RNAs, three volumes of 100% ethanol and linear acrylamide (VWR) were used instead of isopropyl alcohol, and incubation time was also increased to overnight at  $-20^\circ\text{C}$ . The isolated RNAs were quantified by Qubit microRNA assay kit (ThermoFisher). Small RNA libraries were generated with NEBNext Multiplex Small RNA Library Prep Set for Illumina (NEB). To increase yield and prevent primer/adaptor dimer, 3' SR primer was diluted to 1:5

and increased ligation time to overnight at 16°C. Similar to mRNA-seq library preparation, HS DNA chip and KAPA library quantification kit were used before submitting to sequencing by Illumina NovaSeq 6000 in the Florida State University College of Medicine Translational Science Laboratory.

### 2.13 | RNA-seq data analysis

Raw data for miR-seq were submitted to OASIS online miR analysis tool to identify small RNAs on Human reference genome hg38. Differentially expressed miRNAs were analyzed by both OASIS and miRNet using default settings. RNA-seq data was analyzed by ExpressAnalyst. Genes with counts less than 10, variance less than 10%, and unannotated were filtered and normalized by Log2-counts per million. Differentially expressed genes (DEGs) were identified by DESeq2. Heatmap of globe differential expressed genes and gene-enriched pathways were also visualized by the same online tool.

### 2.14 | In vitro functional assays using an oxygen and glucose-deprived (OGD) stroke model

Human induced forebrain cortical organoids (iFCo) were derived from human iPSCs. After the iPSC passage,  $1 \times 10^4$  cells were seeded into each well of 96-well ultra-low attachment plates (Corning Inc.). Y27632 (iXCells Biotechnologies, San Diego, CA, USA) was added in the DMEM/F12 + B27 medium for the first 24 h. SB431542 (Sigma-Aldrich) and LDN193189 (Sigma-Aldrich) were added into the medium from D1 to D7; starting from D12, growth factor FGF2 (PeproTech, Inc.) was added until D30. To mimic ischemic stroke in vitro, iFCo were deprived of oxygen and glucose using a glucose-free DMEM medium (Gibco) and cultured in a hypoxia incubator (2% oxygen) (BioSpherix Ltd., Parish, NY). After 3h, the iFCo were recovered with the glucose-containing medium in a normoxia incubator for 18 h. At the same time, EVs from the three culture conditions were added at different doses: 300, 1000, and 3000 particles/cell. PBS was added as a control. The cells with EV treatments were then analyzed.

### 2.15 | Biochemical assays

#### 2.15.1 | 2,5-diphenyl-2H-tetrazolium bromide (MTT) assay

As described previously (Chen et al., 2023), the organoids were incubated with 5 mg/mL MTT solution for 3 h. Then, the formazan crystals were centrifuged and hydrolyzed by dimethyl sulfoxide. Afterwards, the pink solution was read at 570 nm by the microplate reader (BioRad Laboratories, Hercules, CA, USA).

#### 2.15.2 | Caspase 3/7 assay

The Caspase 3/7 assay was performed as described in the manufacturer's protocol. Briefly, Caspase-Glo 3/7 Reagent (Promega, Madison, WI, USA) was added as a 1:1 ratio to the medium containing iFCo. Organoids were incubated at room temperature in the dark for 3 h, and then the signals were measured by a microplate reader (BioRad Laboratories).

#### 2.15.3 | Reactive oxygen species (ROS) assay

Briefly, iFCo were dissociated into single cells by Accutase. After washing, the cells were treated with 25  $\mu$ M carboxy-H<sub>2</sub>DCFDA (Invitrogen). After 30 min incubation at 37°C (protected from light), the cells were washed and resuspended in PBS for flow cytometry.

### 2.16 | Statistical analysis

Experimental results were expressed as means  $\pm$  standard deviation (SD). Statistical comparisons were performed by one-way ANOVA and Tukey's post hoc test for multiple comparisons, and significance was accepted at  $p < 0.05$ . For comparisons of two conditions, a Student's *t*-test was performed for the statistical analysis.

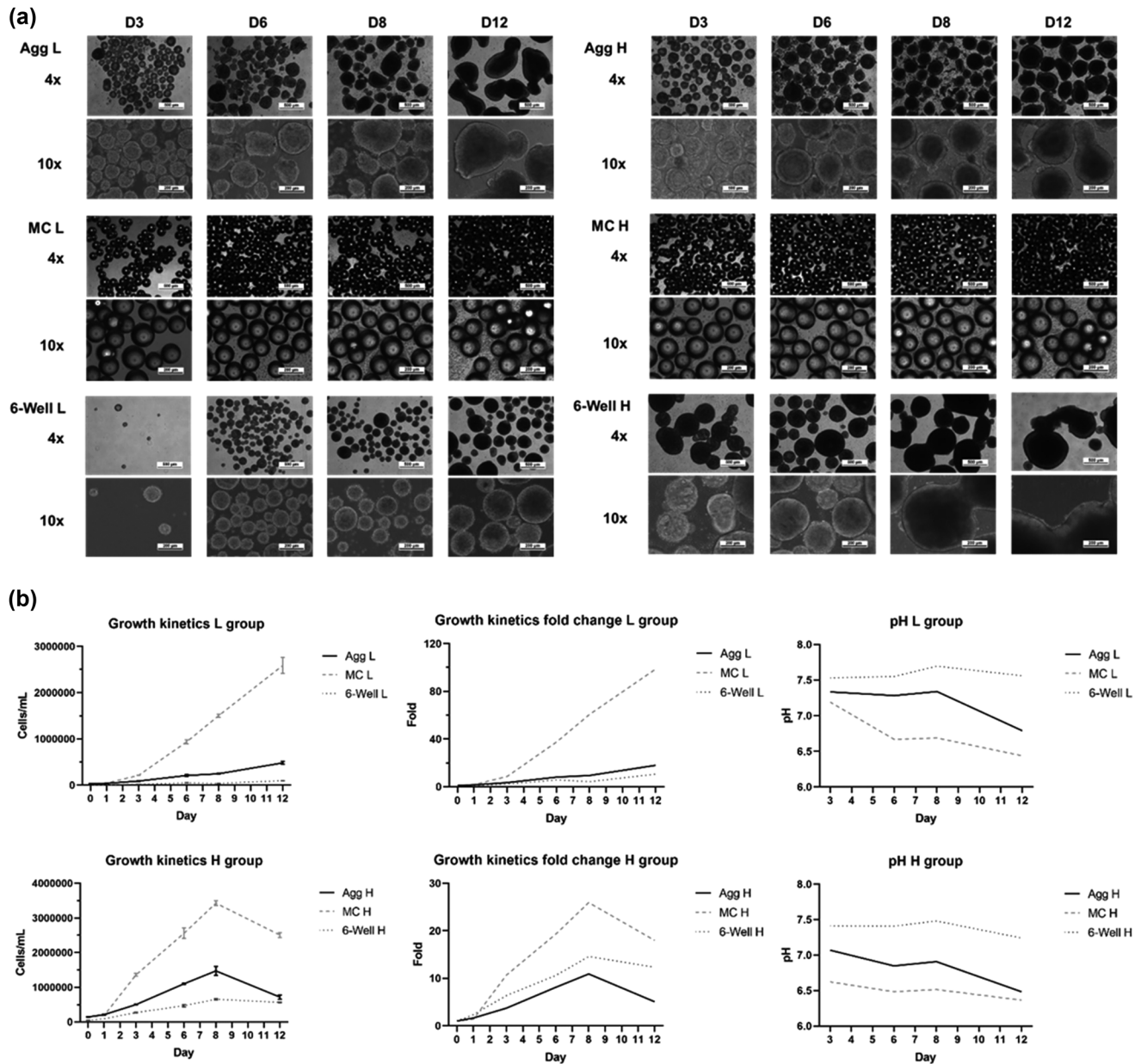


**FIGURE 2** Forebrain spheroid differentiation from human iPSCs on microcarriers and as aggregates in VWBRs (Run 2 data). (a) Culture morphology over time. (b) Cell density, expansion fold, and pH kinetics. H, high seeding density; L, low seeding density. Scale bar of 4x: 500  $\mu\text{m}$ . Scale bar of 10x: 200  $\mu\text{m}$ .

### 3 | RESULTS

#### 3.1 | Forebrain spheroid differentiation of human iPSCs in the VWBR

The experiments were performed as illustrated in Figure 1. The differentiation of forebrain spheroid from human iPSCs in VWBRs was performed for three runs. Run 2 results were shown as representative data. Morphology images showed that the Agg L group became larger than the 6-well L group at D12 ( $\sim 800 \mu\text{m}$  vs.  $500 \mu\text{m}$ ), but the aggregates in the Agg H group were slightly smaller ( $\sim 400 \mu\text{m}$ ) than the 6-well H group all the time (Figure 2a). Aggregate merging was observed for Agg L and 6-well H groups, but Agg H maintained a relatively uniform size of aggregates. Microcarriers with cells formed clumps/clusters during cell growth. Growth kinetics demonstrated that microcarriers greatly promoted cell growth, especially when cells were seeded at lower density, with the fold increase of cell number at  $\sim 100$  (Figure 2b). The Agg and 6-well conditions showed similar growth rates at  $\sim 20$  fold, no matter the dynamic or static environment. Cells in the L group kept growing from D8 to D12, but cells in the H group reached maximum numbers at D8, maybe because the oxygen and nutrients became limiting factors. pH values were consistent with the cell growth curves, with the lower pH (from 7.5 to 6.5) at higher cell densities.



Similar to Run 2, the morphology of Agg L from Run 1 and Run 3 (Figures S1a and S2a) presented a larger or comparable size than 6-well L, but the dynamic Agg H condition showed a smaller size than the static 6-well H condition. The growth kinetics of Run 1 followed a similar pattern to Run 2 (Figure S1b). Results from Run 3 showed that all three culture conditions had a similar fold increase of cell growth (10–17 fold), maybe because of the cluster formation for the MC group (Figure S2b). The quantification of the aggregate size of three runs was  $\sim 500 \mu\text{m}$  (Figure S3).

After harvesting at D12, cells from the three conditions were replated for another 12 days (day 24) to evaluate the differentiation potential. Immunocytochemistry revealed the presence of neural progenitor markers Nestin, PAX6, and SOX2, cortical layer markers TBRI and FOXG1, and neuronal marker  $\beta$ -tubulin III (Figure S4). Flow cytometry quantification showed that the cells at D24 highly expressed TBRI and Nestin (>99%), as well as PAX6 (87.8%–97.7%), but slightly expressed FOXG1 (13.2%–19.2%) (Figure S5). However, for  $\beta$ -tubulin III and SOX2, 6-well showed moderate expression (38.1% and 45.0%), Agg and MC showed about two-fold higher levels of expression (>75.2% and >85.4%).

### 3.2 | Metabolite, metabolism, and EV biogenesis analysis of human iPSCs in the VWBR

Metabolism analysis showed that MC consumed the most glucose and generated the most lactate, 6-well had the least consumption and generation, and Agg was between MC and 6-well conditions (Figure 3a). The metabolite kinetics were consistent with the pattern of cell growth kinetics (Figure 2b). Agg and MC groups showed a ratio of lactate to glucose around 1.5, indicating more aerobic metabolism. The 6-well H showed values between 2 and 3, indicating anaerobic metabolism. 6-well L was not included in the figure because its glucose and lactate levels were below the detection limit due to the low cell numbers. Similarly, for the glutamine consumption and  $\text{NH}_4^+$  generation, MC was the most and 6-well was the least (Figure 3b). The ratios of glutamine to  $\text{NH}_4^+$  for Agg and MC were around 1.0, while 6-well H showed values between 1.5 and 2.5. When normalizing the metabolites to cell numbers (Figure 3c), Agg L and MC H had the lowest and highest number of cells, respectively, and their normalized consumption and generation were the highest and lowest correspondingly. At D12, 6-well H generated lactate and  $\text{NH}_4^+$  with a similar amount to the Agg H group, but its glucose and glutamine consumption were only half of Agg H. The high values of lactate/glucose and glutamine/ $\text{NH}_4^+$  ratios in 6-well compared to Agg and MC conditions indicate that the static culture and VWBR have distinct different cellular metabolism. Agg and MC maintained stable  $\text{K}^+$  and  $\text{Ca}^{2+}$  levels, but 6-well had higher levels and kept releasing  $\text{K}^+$  and  $\text{Ca}^{2+}$  (Figure 3d).

For Run 1 metabolite analysis, glucose and glutamine consumption, lactate and  $\text{NH}_4^+$  generation,  $\text{K}^+$  and  $\text{Ca}^{2+}$  concentrations followed a similar pattern as Run 2 (Figure S6a,b). Lactate/glucose ratios were low at D3 due to the small amount of lactate generation. 6-well H exhibited high lactate/glucose ratio at D6–D12 and high  $\text{NH}_4^+$ /glutamine ratio at D12 as in Run 2 (Figure S6c). For Run 3, glucose and glutamine consumption, lactate and  $\text{NH}_4^+$  generation, lactate/glucose ratio,  $\text{NH}_4^+$ /glutamine ratio, as well as  $\text{K}^+$  and  $\text{Ca}^{2+}$  concentration changes followed a similar pattern as Run 1 and Run 2 (Figure S7). Taken together, the VWBRs result in different cellular metabolism from static differentiation.

### 3.3 | Transcriptome analysis of the differentiated cells

Transcriptome analysis based on Next Generation Sequencing (NGS), that is, mRNA-seq, was performed for the differentiated forebrain spheroids (Figure 4 and Figure S8). Principal component analysis (PCA) plot showed the distinct clusters of 6-well, Agg, and MC cells (Figure 4a). Heatmap analysis further reveals the differences among the three conditions, each condition had its unique gene profiles (Figure 4b). The DEGs were compared between Agg versus 6-well and shown in the volcano plot (Figure 4c). There were 1562 down-regulated genes and 1736 up-regulated genes in Agg. Pathway network analysis showed that the DEGs of Agg versus 6-well were involved in 66 identified pathways (Figure 4d). The metabolism-associated genes *HK1* (−0.751), *HK2* (−2.135), *PDK1* (−2.677), etc., were much lower for Agg versus 6-well ( $\log_2\text{FC}$ ,  $\text{FC}$  = fold of change), indicating that the 6-well group had more anaerobic metabolism with glycolysis pathway than Agg group. EV biogenesis genes *TSG101* (0.216), *STAM2* (0.159), and *SMPD2* (0.135) were slightly higher or comparable in the Agg group. The neuronal cell genes *MAP2* (0.166) and *TUBB3* (−0.671) had mixed results. The top 20 pathways include extracellular matrix (ECM)-receptor interaction, PI3K-Akt signaling pathway, metabolic pathways, axon guidance, focal adhesion, HIF-1 signaling pathway, glycolysis/gluconeogenesis, Hippo signaling pathway, MAPK signaling pathway, lysosome, etc. (Table 1).

When comparing to MC, there were 3431 down-regulated genes and 3385 up-regulated genes in Agg (Figure 4e). The EV biogenesis genes *TSG101* (−0.104), *STAM2* (0.158), and *SMPD3* (−0.195) were comparable for Agg versus MC ( $\log_2\text{FC}$ ,  $\text{FC}$  = fold of change). *CD9* (−0.373), *CD63* (−0.846), and *CD81* (−0.323) were slightly higher for MC group. The neuronal cell genes *MAP2* (0.295) and *TUBB3* (−0.222) were comparable. However, for forebrain regional-specificity, deep cortical layer VI marker *TBRI* (0.970) was slightly higher for Agg and superficial layer II–IV marker *SATB2* (0.129) was comparable. Ventral forebrain marker *DLX1* (3.236) was much higher for Agg. But the cortical forebrain marker at early development *FOXG1* (−4.749) was much higher for MC. Moreover, Agg group had higher expression levels for genes of oligodendrocyte progenitors, *OLIG1* (1.313), *OLIG2* (1.335)

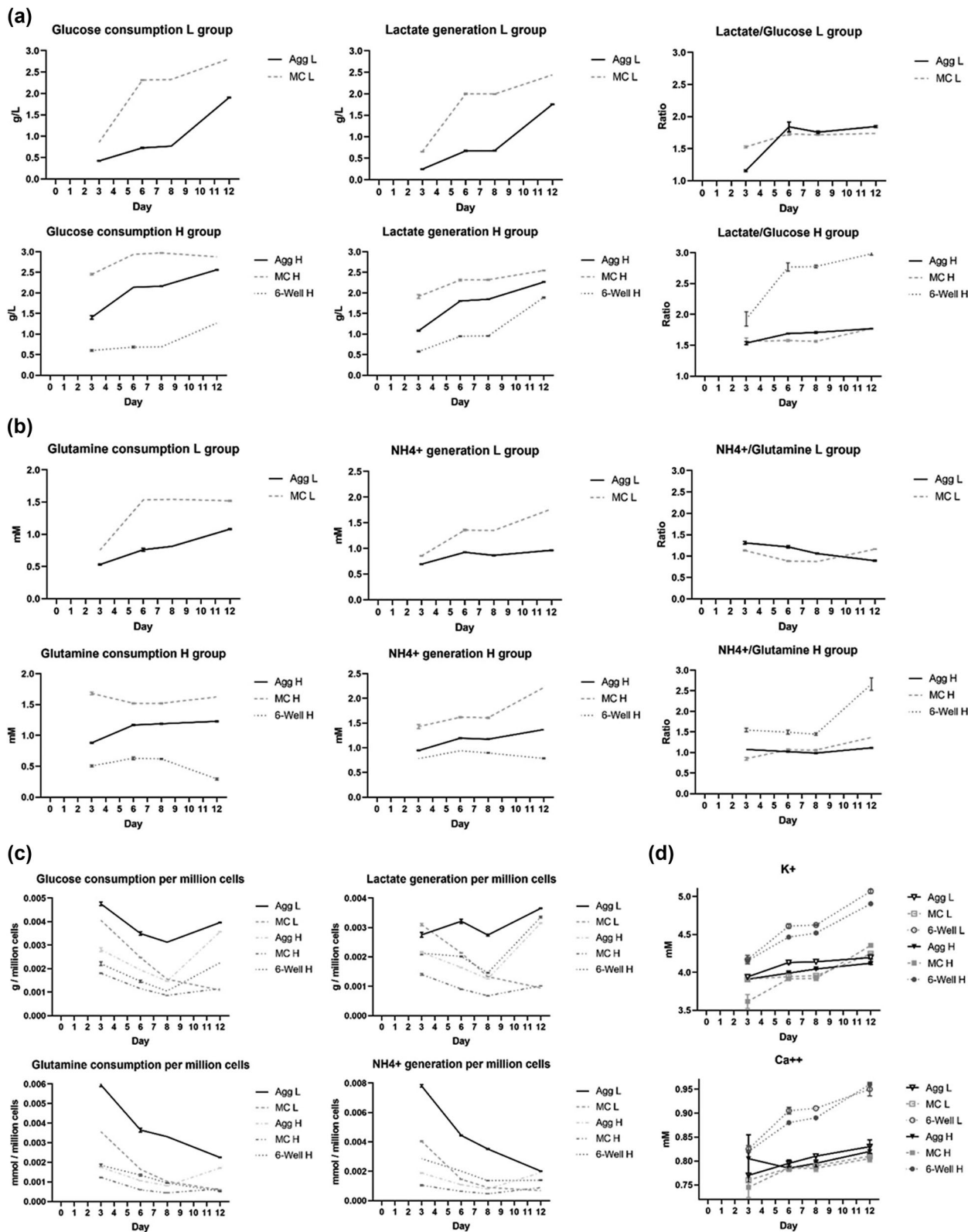


**FIGURE 3** Metabolite analysis of human iPSC-derived forebrain spheroids in VWBRs. (a) Changes in glucose consumption, lactate generation, and the ratio of lactate generation to glucose consumption. (b) Changes in glutamine consumption, NH<sub>4</sub><sup>+</sup> generation, and the ratio of NH<sub>4</sub><sup>+</sup> generation to glutamine consumption. (c) Metabolite concentrations normalized to cell numbers. (d) Changes in K<sup>+</sup> and Ca<sup>2+</sup> over time.

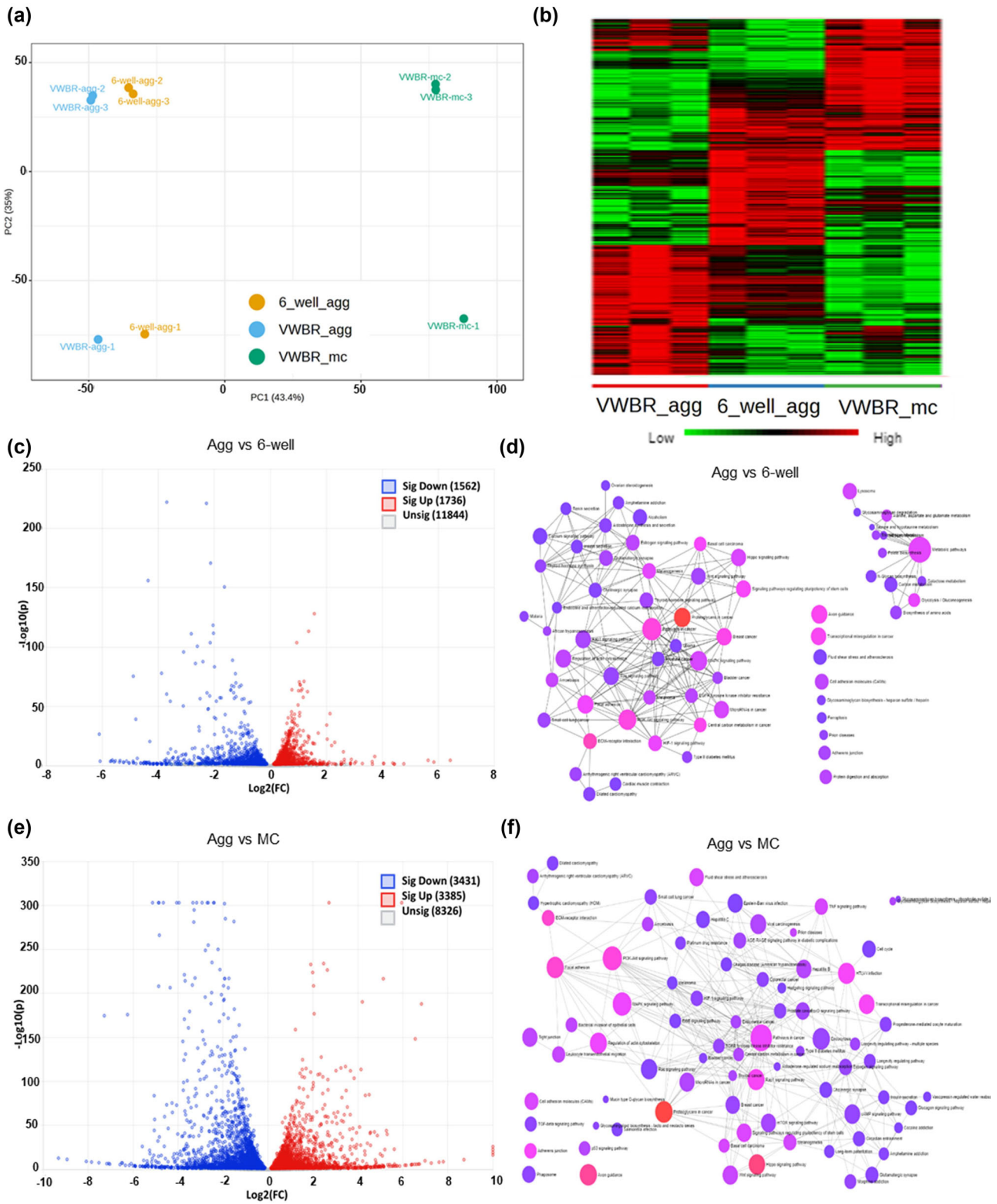


**FIGURE 4** mRNA sequencing of cells grown in the three culture conditions. (a) PCA plot to show the cluster of Agg, MC, and 6-well. (b) Heatmap illustration of top DEGs among the three culture conditions. (c, e) Volcano plot to show the comparison of DEGs between two culture conditions. (d, f) Network plots for gene set enrichment analysis.

**TABLE 1** Top 20 KEGG pathway from DEGs (Agg vs. 6-well).

Pathway	Total	Expected	Hits	p-value	FDR
Proteoglycans in cancer	178	38.8	73	5.04E-09	1.60E-06
ECM-receptor interaction	71	15.5	35	2.78E-07	4.40E-05
Pathways in cancer	451	98.2	140	2.16E-06	0.000189
PI3K-Akt signaling pathway	286	62.3	96	2.38E-06	0.000189
Breast cancer	130	28.3	51	4.68E-06	0.000297
Central carbon metabolism in cancer	58	12.6	28	7.12E-06	0.000357
Axon guidance	177	38.6	64	7.89E-06	0.000357
Transcriptional misregulation in cancer	143	31.1	54	9.41E-06	0.000373
Signaling pathways regulating pluripotency of stem cells	124	27	48	1.34E-05	0.000474
Basal cell carcinoma	58	12.6	27	2.39E-05	0.000756
Focal adhesion	184	40.1	64	3.22E-05	0.000927
HIF-1 signaling pathway	89	19.4	36	5.28E-05	0.00131
Glycolysis/Gluconeogenesis	48	10.5	23	5.37E-05	0.00131
Metabolic pathways	1180	258	311	7.16E-05	0.00161
Melanogenesis	87	18.9	35	7.61E-05	0.00161
Hippo signalling pathway	146	31.8	51	0.000173	0.00332
MAPK signalling pathway	269	58.6	84	0.000178	0.00332
MicroRNAs in cancer	147	32	51	0.000209	0.00368
Lysosome	112	24.4	41	0.000234	0.00391
Alanine, aspartate and glutamate metabolism	32	6.97	16	0.000399	0.00632

and *SOX10* (1.334), astrocyte markers *SI00B* (2.714), *SLCIA2* (2.147), *AQP4* (2.099) and *SOX9* (0.637), microglia-associated genes *TMEM119* (2.890) and *PROSI* (0.959). It also has much higher WNT pathway genes, such as *WNT4* (12.084) and *WNT3A* (1.732). MC had higher genes of growth factors such as *VEGFA* (−1.117) and *TGFBI* (−1.088). These results indicate that the Agg group displayed more complex forebrain patterning with more cellular diversity compared to MC group. For the DEGs of Agg versus MC, there were 79 identified pathways (Figure 4f). The top 20 pathways include the hippo signaling pathway, axon guidance, ECM-receptor interaction, Rap1 signaling pathway, HTLV-I infection, adherens junction, regulation of actin cytoskeleton, cell adhesion molecules, fluid shear stress and atherosclerosis, TNF signaling pathway and Wnt signaling pathway (Table 2).

Gene expression of autophagy, EV biogenesis, and metabolism of the differentiated cells at D12 was determined (Figure 5). MC and Agg groups reduced some genes differentially related to cellular autophagy compared to 6-well group, such as *TFEB*, *BECNI*, *LAMP1* and *AMPK*, especially for high-density conditions (Figure 5a). For EV biogenesis in endosomal sorting complex required for transport (ESCRT) independent and dependent pathways, Agg and MC groups showed higher expression of some genes such as *Rab7a*, *Rab27b*, *HRS* and *STAM1/2* than the 6-well group, especially for MC condition. This trend was more significant in the L group. The Agg and MC exhibited less active glycolytic activity with about 2-fold lower expression of *HK2*, *LDHA*, *PDK1* and *PKM2* than the 6-well group (Figure 5b). For pentose phosphate pathway (PPP) activity, the MC group had the lowest gene expression (i.e., *6PGD*, *G6PD* and *TALDO1*), while the Agg and 6-well had comparable expression levels. These results are consistent with the metabolite analysis.

For neural differentiation, Agg L and MC L had higher levels of *Nestin* and *PAX6* than 6-well L, indicating that VWBR microenvironment promotes differentiation into NPCs. MC L had lower *TUBB3* and higher *SOX2*, which indicates that the cells may have a higher pluripotency level (more neural progenitors) and less mature neurons than the other two conditions. Similarly, MC H had higher *Nestin*, lower *TBRI* (deep cortical layer VI marker), and higher *SOX2* expression than the other two conditions (Figure 5b). Five glycolytic pathway genes (*HK1/2*, *LDHA*, *PDK1* and *PKM*) and two neural differentiation genes (*FOXG1* and *PAX6*) were selected from transcriptome analysis of the H group (Figure 5c). Consistent with RT-qPCR results, Agg and MC groups exhibited significantly decreased glycolytic gene activity and a lower level of *FOXG1* compared to the static culture.

### 3.4 | EV isolation and characterization

EVs were isolated from D12 media of all conditions. The EV size and concentrations were measured by NTA: the mean sizes were ~300 nm, and the mode sizes were ~200 nm (Figure 6a,b). Different cultural conditions did not show a significant influence on

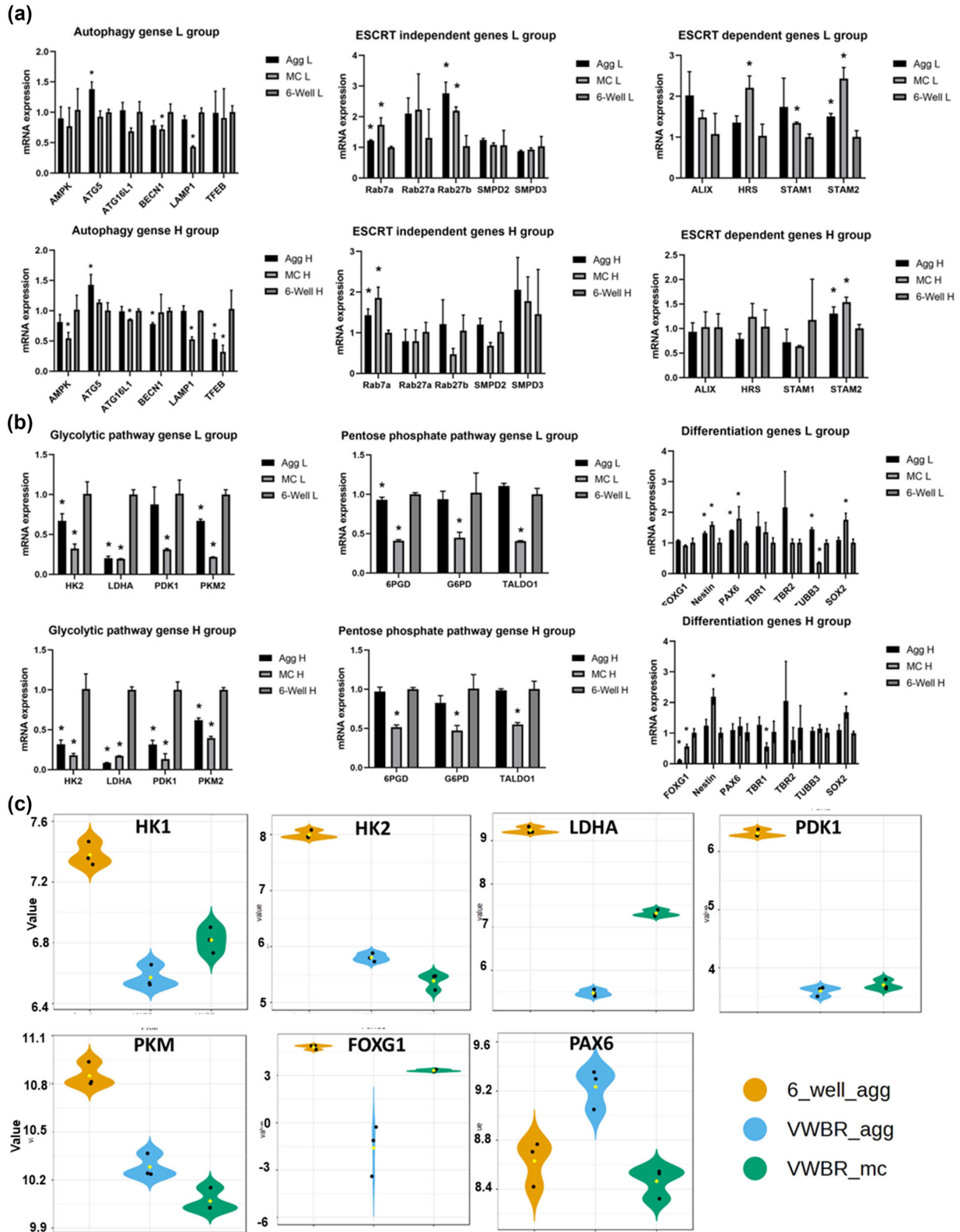


**FIGURE 5** Neural differentiation, EV biogenesis, and metabolic pathway analysis by RT-qPCR. (a) Autophagy genes, ESCRT-independent and -dependent genes. (b) Glycolytic genes, pentose phosphate genes and differentiation genes. ESCRT, endosomal sorting complex required for transport. (c) Genes selected from mRNA-Seq dataset. \* indicates  $p < 0.05$ .

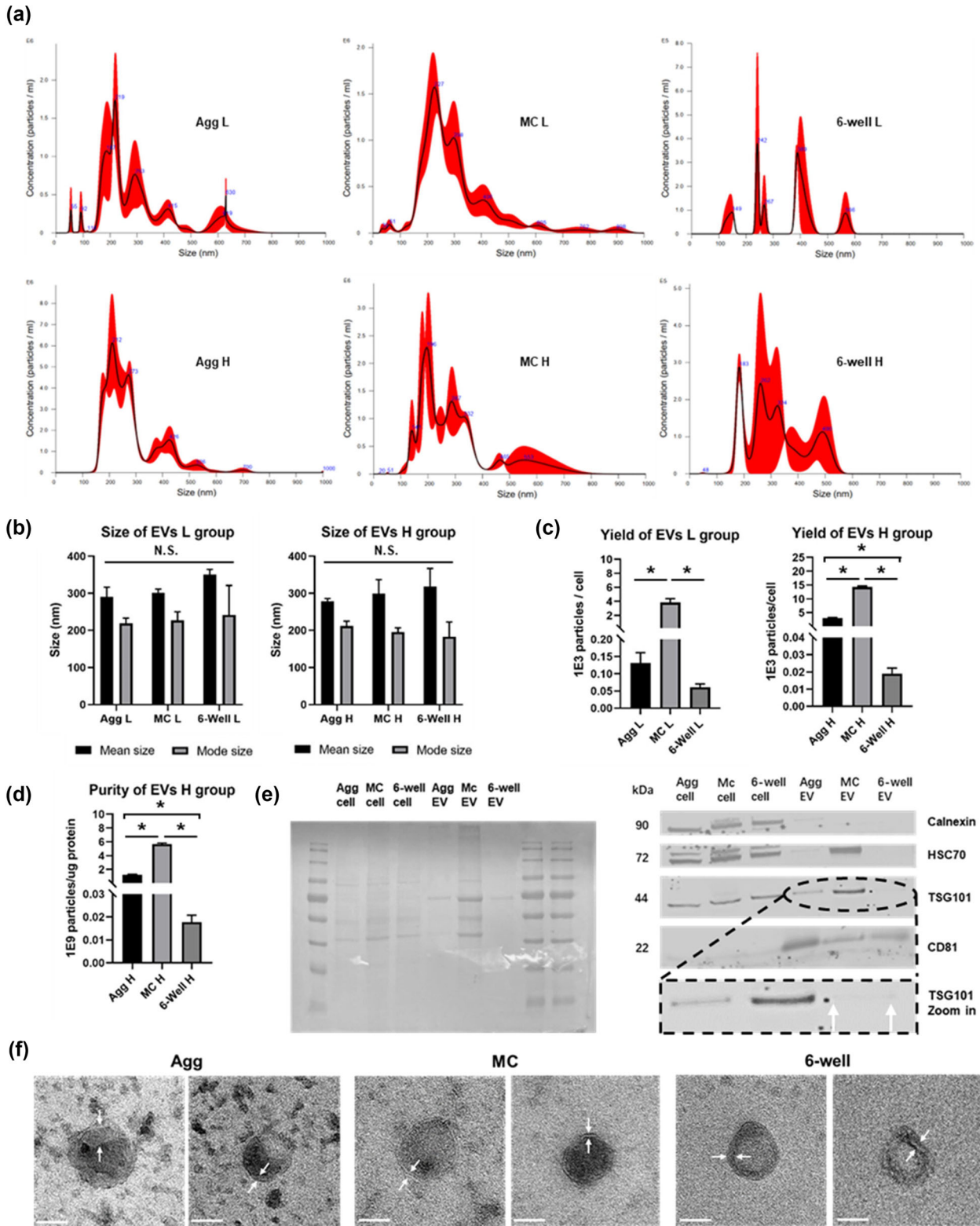


**FIGURE 6** EV isolation and characterizations (Run 2 data). (a) The representative particle size distribution measured by nanoparticle tracking analysis. (b) EV mean and mode sizes. (c) EV particle numbers normalized to cell numbers. (d) EV particle numbers normalized to protein amounts. (e) Western blot assay of exosomal markers (right) and Ponceau S staining of gel (left). (f) TEM images to show exosome morphology. The double layer was indicated by a pair of pointing arrows. Scale bar: 200 nm. \* indicates  $p < 0.05$ . N.S. not significant.

**TABLE 2** Top 20 KEGG pathways from DEGs(Agg vs. MC).

Pathway	Total	Expected	Hits	p-value	FDR
Proteoglycans in cancer	179	80.6	123	1.04E-10	3.31E-08
Hippo signaling pathway	146	65.7	103	3.26E-10	5.17E-08
Axon guidance	177	79.7	119	1.71E-09	1.81E-07
ECM-receptor interaction	71	32	54	9.45E-08	7.49E-06
Focal adhesion	184	82.8	118	1.19E-07	7.56E-06
PI3K-Akt signaling pathway	286	129	171	2.89E-07	1.52E-05
Transcriptional misregulation in cancer	143	64.4	92	2.33E-06	9.41E-05
Rap1 signaling pathway	182	81.9	113	2.37E-06	9.41E-05
HTLV-I infection	185	83.3	114	3.63E-06	0.000128
Adherens junction	71	32	51	4.13E-06	0.000131
Pathways in cancer	451	203	248	1.01E-05	0.000269
Regulation of actin cytoskeleton	188	84.6	114	1.07E-05	0.000269
MAPK signaling pathway	269	121	156	1.10E-05	0.000269
Signalling pathways regulating pluripotency of stem cells	124	55.8	78	4.34E-05	0.000982
Cell adhesion molecules (CAMs)	104	46.8	67	4.99E-05	0.00103
Fluid shear stress and atherosclerosis	117	52.7	74	5.18E-05	0.00103
TNF signaling pathway	90	40.5	59	6.59E-05	0.00117
Basal cell carcinoma	58	26.1	41	6.63E-05	0.00117
Melanogenesis	87	39.2	57	8.94E-05	0.00149
Wnt signaling pathway	143	64.4	86	0.000185	0.00294

EV size. Yields were calculated by normalizing EV numbers to cell numbers (Figure 6c). For both L and H groups, MC exhibited the highest yield (80-fold of the 6-well for L; 750-fold of the 6-well for H); Agg showed moderate yield (2.5-fold of the 6-well for L; 240-fold of the 6-well for H); 6-well had the lowest yield. Purities were calculated by normalizing EV numbers to protein amounts (Figure 6d). Compared to 6-well condition, MC group had a purity of 300-fold higher and the Agg group was 100-fold higher. Western blot assay confirmed the expression of exosomal markers (Figure 6e). Calnexin (the negative exosome marker) was enriched in cell lysates, but not shown in the EVs; HSC70, TSG101 and CD81 are positive exosome markers that were shown in the EVs. The 6-well EV sample had low expression of HSC70 and TSG101, probably due to the low total protein amount or the impurity. TEM images showed that these EVs presented doubled-layered cup-shaped morphology (Figure 6f).

Size distributions of EVs from Run 1 and Run 3 were analyzed (Figures S9 and S10). Run 1 and Run 3 EVs had similar mean and mode sizes as Run 1, but Agg L EVs and MC L EVs demonstrated significantly smaller mode sizes than 6-well L EVs (200 nm vs. 250 nm). Consistent with the yield and purity in Run 2, Run 1 and Run 3 revealed that the MC group generated the most EVs with the highest purity, the Agg group was in between, while the 6-well group generated the least EVs with the lowest purity.

### 3.5 | EV cargo analysis—proteomics and miRNA-sequencing

Multi-omics data analysis was performed to reveal the EV cargo profile and composition (Figure S11). The protein cargo of the isolated EVs was analyzed by LC-MS/MS-based proteomics (Figure 7 and Figure S12). PCA plot showed distinct clusters of the Agg, MC, and 6-well groups (Figure 7a). Especially, both the Agg and MC groups were high in PCI, probably due to their common dynamic growth environment. The differentially expressed proteins (DEPs) are shown in the Venn diagram (Figure 7b). The left figure of Figure 7b shows the presence/absence of proteins in each culture condition. There were 1780 proteins presented in all three conditions. Agg and MC had 283 overlapped DEPs, Agg and 6-well had 50 overlapped DEPs, MC and 6-well had 36 overlapped DEPs. There were less than 50 unique proteins in each culture condition. The right figure of Figure 7b was the high/low expression of proteins in each culture condition. There were 1239 proteins highly expressed in all three conditions. There were 372 DEPs abundant in both the MC and Agg groups but low in the 6-well group, 24 DEPs were high in both Agg and 6-well, and only 7 DEPs were enriched in both MC and 6-well. For DEPs only enriched in single culture condition, there were 378 proteins for Agg, 276 proteins for MC, and 111 proteins for 6-well.

In a volcano plot, the comparison of Agg versus 6-well revealed 914 insignificant proteins, 85 down-regulated DEPs, and 383 up-regulated DEPs (Figure 7c). The DEP-associated pathways were shown in Ridgeline diagram, with the majority shifted to the

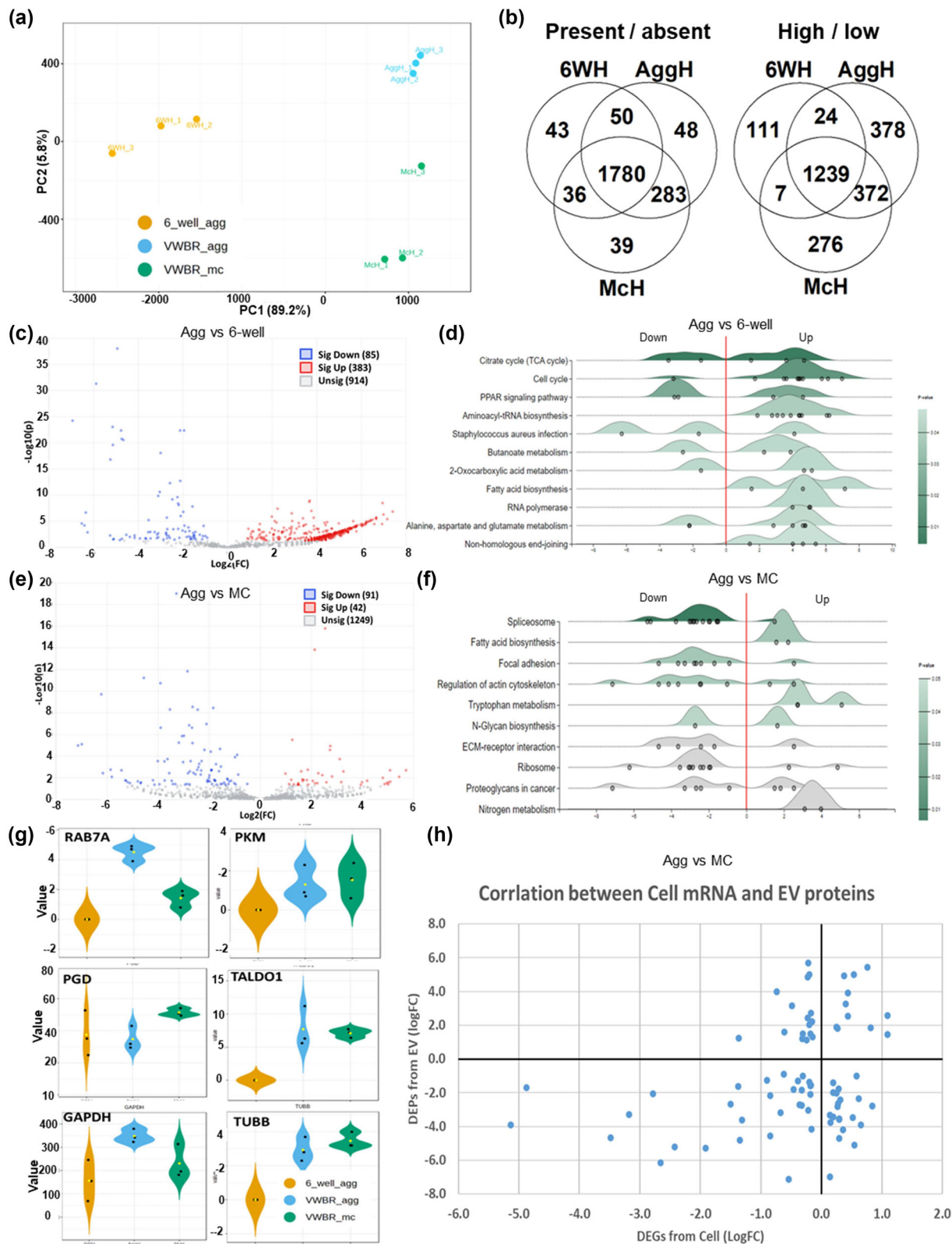


**FIGURE 7** Proteomics analysis of forebrain spheroid EV protein cargo. (a) PCA plot to show the cluster of Agg, MC, and 6-well. (b) Venn diagram of DEPs for the three EV groups. (c, e) Volcano plot to show the comparison of DEPs between two culture conditions. (d, f) Ridgeline diagram of DEP enriched pathways. (g) Proteins selected from proteomics data to match RT-qPCR data as in Fig.5. (h) Correlation between cell mRNA sequencing data and EV proteomics.



**TABLE 3** Top 15 miRNAs from miRNA sequencing.

Agg cell	MC cell	Agg EV	MC EV
hsa-miR-302a-5p	hsa-miR-302a-5p	hsa-miR-302a-5p	hsa-miR-302a-5p
hsa-miR-148a-3p	hsa-miR-21-5p	hsa-miR-21-5p	hsa-miR-21-5p
hsa-miR-302b-3p	hsa-miR-302b-3p	hsa-miR-148a-3p	hsa-miR-302b-3p
hsa-miR-21-5p	hsa-miR-148a-3p	hsa-miR-302b-3p	hsa-miR-148a-3p
hsa-miR-92a-3p	hsa-miR-92a-3p	hsa-miR-92a-3p	hsa-miR-92a-3p
hsa-miR-151a-3p	hsa-miR-151a-3p	hsa-miR-151a-3p	hsa-miR-30a-5p
hsa-miR-30d-5p	hsa-miR-30d-5p	hsa-miR-30d-5p	hsa-miR-30d-5p
hsa-miR-7-5p	hsa-miR-7-5p	hsa-miR-30a-5p	hsa-miR-151a-3p
hsa-miR-30a-5p	hsa-miR-30a-5p	hsa-miR-7-5p	hsa-miR-7-5p
hsa-miR-363-3p	hsa-miR-363-3p	hsa-miR-26a-5p	hsa-miR-26a-5p
hsa-miR-26a-5p	hsa-miR-26a-5p	hsa-miR-363-3p	hsa-miR-302a-3p
hsa-miR-101-3p	hsa-miR-101-3p	hsa-miR-302a-3p	hsa-miR-363-3p
hsa-miR-25-3p	hsa-miR-302a-3p	hsa-miR-302c-3p	hsa-miR-302c-3p
hsa-miR-302a-3p	hsa-miR-25-3p	hsa-miR-20b-5p	hsa-miR-20b-5p
hsa-miR-148b-3p	hsa-miR-148b-3p	hsa-miR-302d-3p	hsa-miR-302d-3p

right, that is, up-regulated in the Agg condition (Figure 7d). These pathways include the citrate cycle involved in metabolism, PPAR signaling pathway, alanine, aspartate and glutamate metabolism, etc., the cell cycle, aminoacyl-tRNA biosynthesis, fatty acid biosynthesis, RNA polymerase and non-homologous end-joining. The comparison between Agg and MC showed 1249 insignificant proteins, 91 down-regulated DEPs and 42 up-regulated DEPs (Figure 7e). Those down-regulated DEPs were mainly involved in functions such as spliceosome, focal adhesion and regulation of actin cytoskeleton (Figure 7f). Those up-regulated DEPs were involved in fatty acid biosynthesis and tryptophan metabolism. At the protein level, PKM, PGD and GAPDH showed comparable expressions; while RAB7A (involved in EV biogenesis), TALDO1, and TUBB tended to be more abundant in Agg and MC culture conditions (Figure 7g), and these results are consistent with their mRNA level in parent cells (Figure 5). The transcriptome of the parent cells based on mRNA sequencing data and EV proteomics data of Agg versus MC were compared to identify the correlation (Figure 7h). There were 78 DEGs/DEPs overlapped in these two datasets. Eleven DEGs/DEPs were both up-regulated, and 30 DEGs/DEPs were both down-regulated. Sixteen DEGs were expressed lower in Agg, but the corresponding proteins were higher. Twenty-one DEGs were enhanced in Agg but the corresponding DEPs were lower. A weak increasing trend of EV DEPs with the parent cell DEGs was observed.

miRNA sequencing was performed to analyze miRNA cargo in the EVs as well as the parent cells in order to reveal the miRNA packaging process. The 6-well group was not included due to the low EV amount. The PCA plot showed distinct clusters of parent cells from the corresponding EVs (Figure 8a). For the total four groups, the parent cells had more mature miRNAs identified than the corresponding EVs: 400–500 for Agg cell versus 200–300 for Agg EV, 300–600 for MC cell versus 200–300 for MC EV (Figure 8b). Heatmap analysis further revealed the differences among the four conditions: Agg and MC cells shared more similarities, and their EVs were more similar (Figure 8c). The top 15 miRNAs in the parent cells and the EVs are shown in Table 3. They were basically a similar set of miRNAs but varied in their amounts in each set, including miR-302a, 302b, 148a, 21, 92a, 151a, 30d, 30a, 7, 363, 26a, 302c, 302d and 20d. In the parent cells, two major miRNAs different between Agg and MC were miR-30d-5p and miR-21-5p. miR-30d-5p was more enriched in Agg, and miR-21-5p was more enriched in MC group. In the EVs, two major miRNAs different between Agg and MC groups were miR-30a-5p and miR-21-5p, both were more abundant in MC group (Figure 8d).

When comparing DEGs between EVs and their parent cells in MC group, heatmap and volcano plot showed that 67 differentially expressed miRNAs were identified: 36 of them were down-regulated in EVs and 31 were up-regulated in the EVs (Figure 8e,f). The Kyoto Encyclopedia of Genes and Genomes (KEGG) analysis revealed that 45 miRNAs in EVs of the MC group were involved in various pathways, including Wnt signaling, TNF signaling, T cell receptor signaling, apoptosis, cholinergic synapse, regulation of autophagy, antigen processing and presentation, cell adhesion molecules, axon guidance, Jak-STAT signaling, mTOR signaling, ErbB signaling, cell cycle and Hippo signaling pathway, etc. (Figure 8g). When comparing DEGs between EVs and their parent cells in the Agg group, heatmap showed 54 differentially expressed miRNAs and the volcano plot identified 56 miRNAs. Thirty-four were down-regulated in the EVs, and 22 were up-regulated in the EVs (Figure 8h,i). The KEGG analysis revealed that 45 miRNAs were involved in various pathways, including tight junction, dopaminergic synapse,

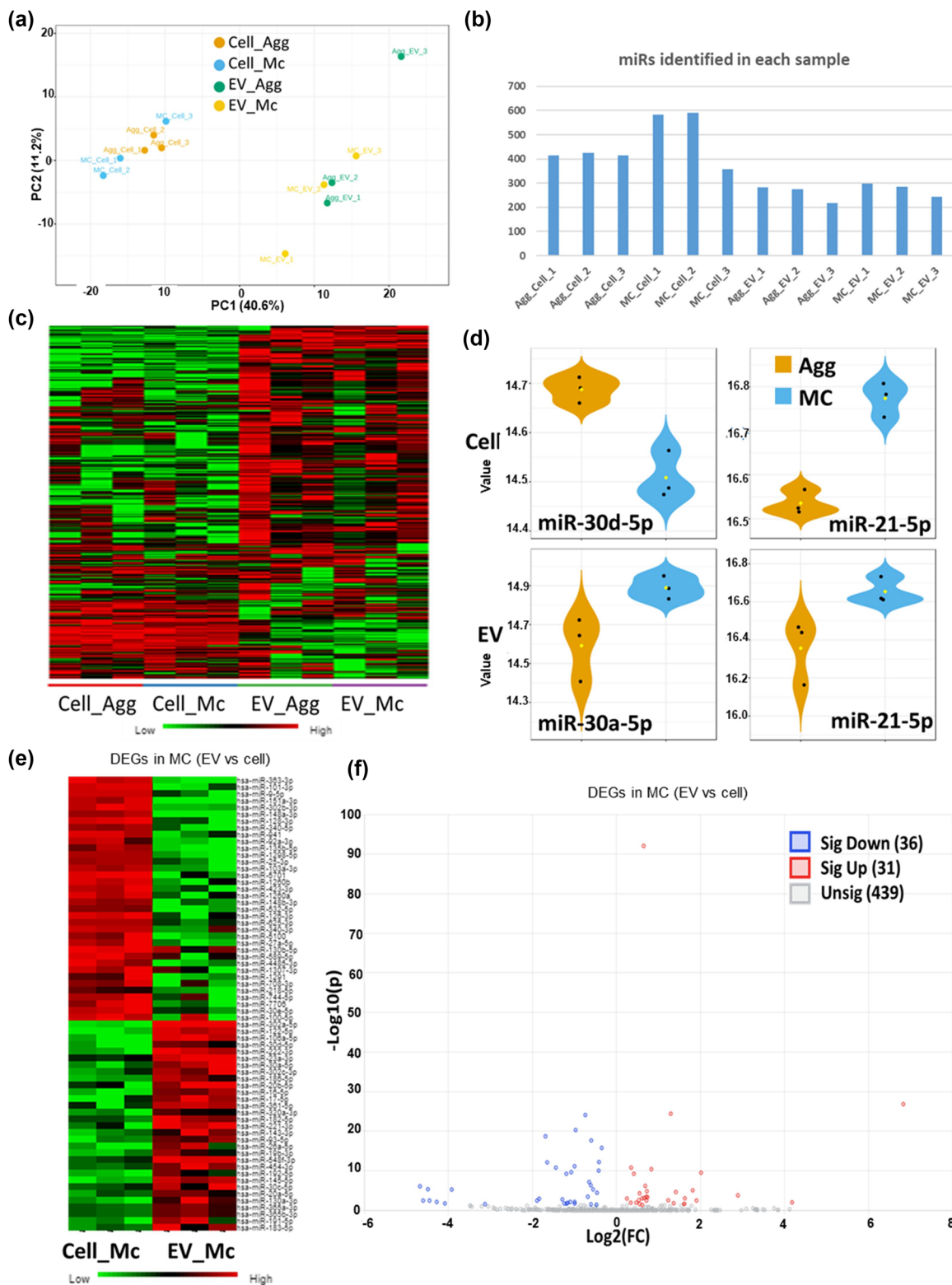


**FIGURE 8** miRNA sequencing of forebrain spheroid EV miRNA cargo. (a) PCA plot to show the cluster of Agg cell, MC cell, Agg EV and MC EV. (b) The count of miRNAs identified in each sample. (c) Heatmap illustration of top DEGs among the four conditions. (d) DEGs identified in cells and EVs (Agg vs. MC). (e, h) Heatmap of DEGs in MC and Agg (EV vs. cell). (f, i) Volcano plot of DEGs in MC and Agg (EV vs. cell). (g, j) KEGG pathway analysis for the top miRNAs. Enlarged images are provided for (e), (g), (h) and (j) in supplementary materials.

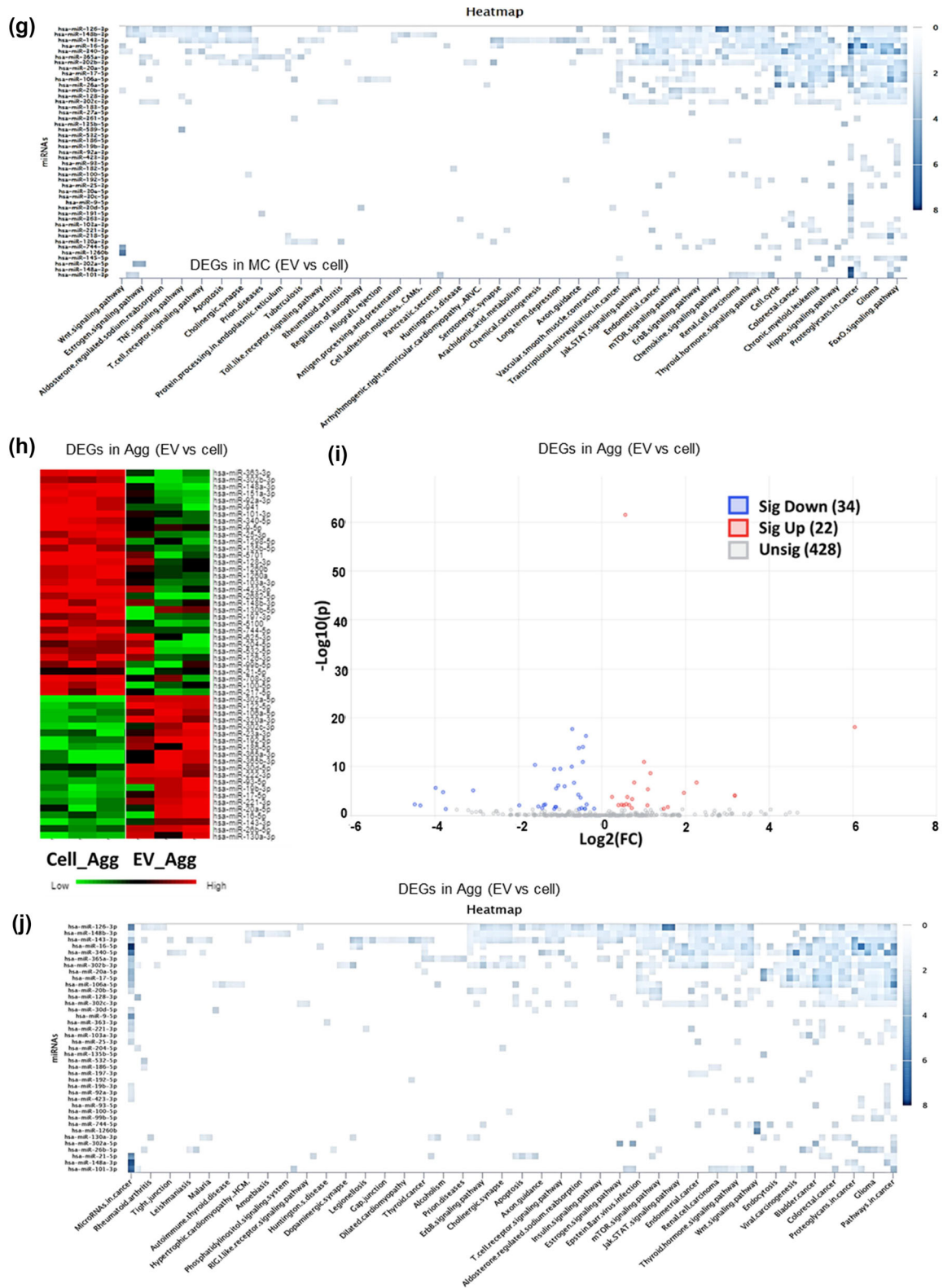


FIGURE 8 Continued

gap junction, ErbB signaling, cholinergic synapse, apoptosis, axon guidance, T cell receptor signaling, mTOR signaling, Jak STAT signaling, and Wnt signaling pathway, etc. (Figure 8j). Enlarged images of 8E, 8G, 8H and 8I are shown in Figure S13.

### 3.6 | In vitro functional analysis

An OGD stroke model was used to evaluate EV therapeutic potentials. Human iFCo derived from iPSCs were carried out under oxygen and glucose deprivation and then treated with EVs from different conditions at different doses (Figure 9 and Figure S14). MTT assays showed that OGD more than 3 h significantly reduced the iFCo metabolic activity (Figure S14a). EV treatment was performed during iFCo recovery from OGD. MTT absorbance readings revealed that 6-well L, MC M and 6-well M enhanced ( $p = 0.001$ ,  $p = 0.022$ ,  $p = 0.033$ , respectively) iFCo metabolic activity in comparison to the PBS vehicle control, while the high EV dose (H) slightly reduced MTT readings. 6-well L showed significantly higher MTT absorbance than Agg L and MC L ( $p = 0.007$  and  $p < 0.001$ ), but there was no difference for VWBR groups versus the static group at medium and high doses. In the Caspase 3/7 assay, Agg L and 6-well L decreased the caspase 3/7 levels, which means the lowered apoptosis activity (Figure S14b). The increased readings of high EV dose treatment intensified apoptosis of iFCo, which is consistent with the MTT results. After EV treatment, the reactive oxygen species (ROS) level of iFCo was detected by flow cytometry (Figure S14c), and no significant differences were observed.

Effects of EV treatment on iFCo OGD stroke model were investigated at the molecular level. For the genes related to the glycolytic pathway, *HK2* was down-regulated by all the EV groups except 6-well M; *LDHA* was up-regulated by all the EV groups except MC M; EVs from Agg L enhanced *PDK1*, but none of the EV groups changed *PKM2* expression (Figure 9a). For the genes related to the pentose phosphate pathway, EVs from Agg L, 6-well L and Agg M groups reduced *6PGD* level; *G6PD* was up-regulated by all the EV groups; *TALDO1* was down-regulated by all the EV groups; *TKL1* was not affected by EV treatment (Figure 9b). For the genes related to the tricarboxylic acid (TCA) cycle pathway, *IDH1*, *IDH2*, *MDH1*, *KGD2* were not affected by EV treatment; *KGD1* was up-regulated by MC M and 6-well M; *PDHAI* was enhanced by 6-well M compared to 6-well L and Agg M (Figure 9c).

The proliferation gene *MKI67* was not influenced by EVs (Figure 9d). The *Casp3* gene was down-regulated by EVs from 6-well L, MC M and 6-well M ( $p < 0.001$ ); but not the *Casp7* gene (Figure 9e). The ROS scavenging gene *CAT* was up-regulated by EVs from 6-well L, Agg M and MC M groups ( $p = 0.005$ ,  $p = 0.002$ ,  $p = 0.007$ , respectively), while *SOD2* was only enhanced by EVs from Agg M ( $p = 0.048$ ) (Figure 9f). For the pro-inflammatory genes, *IL-6* was up-regulated by EVs from 6-well L, Agg M and MC M groups; while *iNOS* was down-regulated by EVs from Agg L, and 6-well L ( $p = 0.029$ ,  $p = 0.008$ ) (Figure 9g). *IL-12 $\beta$*  did not respond to EVs. For the anti-inflammatory genes, Agg L, Agg M and 6-well M enhanced *Arginase-1* expression than 6-well L and MC M; *IL-10* was up-regulated by EVs from all the groups except 6-well L; *TGF- $\beta$*  was elevated only by EVs from MC M (Figure 9h). These results indicate that the EVs mainly promoted anti-inflammatory factors rather than reducing pro-inflammatory factors (Buzas, 2023). Overall, EVs from VWBR cultures demonstrated dose-dependent therapeutic efficacy differentially compared to the static culture at both the cellular and molecular levels (Table S3). A preliminary study on an in vivo rat model of the middle cerebral artery occlusion (MCAO) was performed using MC EVs from high-density culture (Figure S15). A cortical and striatal hyperintense signal indicative of the ischemic lesion was measured over 21 days. A longitudinal reduction in lesion volume calculated based on IH signal was observed for MC EV-treated animal.

## 4 | DISCUSSION

Our previous studies have investigated the VWBR system to produce EVs from human MSCs (Jeske et al., 2023), undifferentiated human iPSCs (Muok et al., 2024), human iPSC-derived retail organoids (Arthur et al., 2023), and natural killer cells (Nathani et al., 2024), following the MISEV 2023 guidelines (Welsh et al., 2024). This study focuses on the EV generation from human forebrain spheroids toward stroke therapy and the knowledge gained should be applicable to other types of iPSC-derived spheroids and organoids.

### 4.1 | VWBR resulted in different metabolism and gene expression compared to static culture

In this study, human forebrain spheroids were derived from iPSCs in dynamic VWBRs as aggregates (Agg) or on microcarriers (MC) to compare to the static aggregate control (6-well). Even though the three culture conditions had the same initial seeding densities (low (L) or high, (H)) of iPSCs, the MC condition greatly improved cell growth, which was proved by cell counting, pH measurement, as well as changes in metabolite concentrations, such as glucose, lactate, glutamine,  $\text{NH}_4^+$ . Agg and 6-well showed similar growth kinetics, but at the metabolic level, Agg shared more similarities (e.g., lactate to glucose ratio, more aerobic metabolism compared to the static control) with MC probably due to their dynamic environment. It has been reported

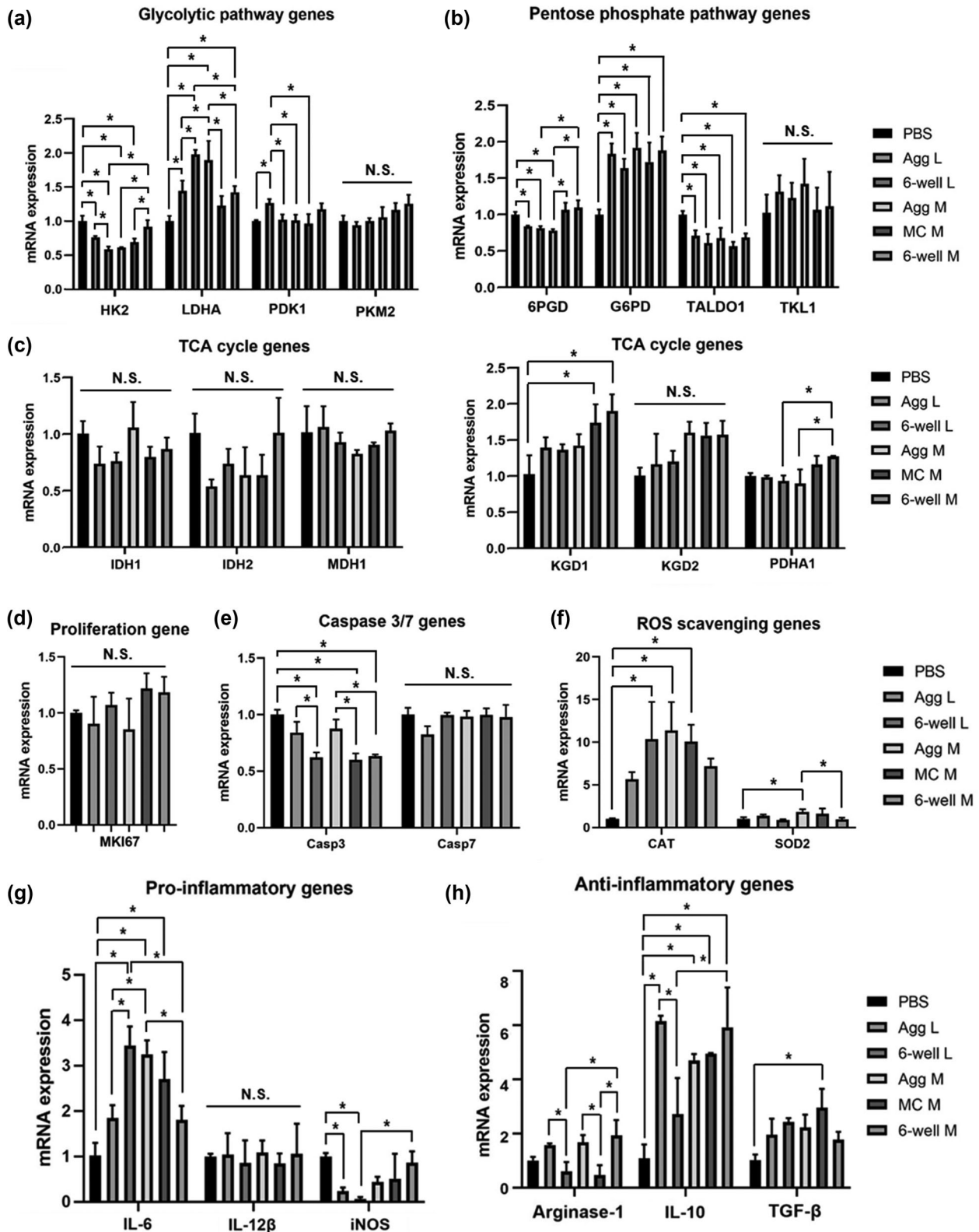


**FIGURE 9** In vitro functional assays in iFCo OGD stroke model for EV therapeutic evaluation. RT-qPCR results of EV treatment after OGD. Genes were involved in carbon metabolism (a–c), proliferation and apoptosis (d, e), ROS scavenge (f) and immune response (g, h). OGD, oxygen and glucose deprivation; ROS, reactive oxygen species; TCA, tricarboxylic acid. \* indicates  $p < 0.05$ . N.S., not significant.

that VWBR greatly improved the expansion of stem cells versus 2D monolayer (Teryek et al., 2023), but the comparison between dynamic and static 3D cultures was rarely studied. In a static environment, the core of aggregates suffers from poor nutrients, wastes and oxygen transfer (Horiguchi & Kino-oka, 2021). Murphy et al.'s study found that the large size of MSC aggregates had a less active metabolism (Murphy et al., 2014, 2017). Consistently in this study, the static 6-well H culture exhibited larger diameters and lower cell-number-normalized glucose consumption than Agg H culture. The smaller size of Agg condition may be attributed to the shear stress in the VWBRs. By adjusting the rotation speed of the impeller, aggregate size can be controlled. For example, faster speed leads to smaller diameters, but cell viability would be impaired as well (Borys et al., 2021). In this study, a low speed of 40 rpm was chosen but provided enough power to suspend cells grown as aggregates and on microcarriers.

Starting from the same seeding densities, MC greatly enhanced cell proliferation compared to Agg. In Borys et al.'s study, iPSCs were inoculated at  $2 \times 10^4$  cells/mL into VWBRs and achieved 31.6-fold expansion under optimized culture conditions (Borys et al., 2020). In a study that grew iPSCs on microcarriers, a  $2.5 \times 10^4$  cells/cm<sup>2</sup> (equivalent to  $1.8 \times 10^5$  cells/mL) seeding density led to a maximum  $1.2 \times 10^6$  cells/mL density and a 6.7-fold expansion (Rodrigues et al., 2018). In Vallabhaneni et al.'s study, aggregate and microcarrier-based iPSC cultures showed 18- and 22-fold expansion, respectively (Vallabhaneni et al., 2023). These studies focused on iPSC expansion rather than differentiation in VWBRs. Moreover, in other studies that employ VWBR for iPSC differentiation, the cells were cultured as aggregates so the microcarrier condition was not investigated (Dadhech et al., 2023; Silva et al., 2021). In this study, iPSC-derived forebrain spheroids on microcarriers showed 26-fold (H) and 99-fold (L) expansion, and the aggregates had 10–20 fold expansion. Such a high proliferation rate of MC culture did not impair their differentiation potential compared to Agg and 6-well conditions.

At the gene level, Agg exhibited more resemblance to 6-well. However, no matter if we compare Agg to 6-well or MC, the differences include ECM-receptor interaction, focal adhesion, cell adhesion molecules, etc. Both shear stress introduced by VWBRs and surface rigidity caused by microcarriers transduce signals to integrin-associated cell-ECM adhesion complexes. The focal adhesions transmit short-range tensile and force, and further induce long-range alterations in cells (Jones et al., 2019; Ray et al., 2015). The influences on cell cycle and differentiation (Jones et al., 2019) may contribute to the differences of Agg versus 6-well or Agg versus MC in signaling pathways regulating pluripotency of stem cells, axon guidance, Wnt signaling pathway, Hippo signaling pathway, PI3K-Akt signaling pathway, etc. RT-qPCR of cellular genes revealed low carbon metabolism activities of MC compared to 6-well, which was consistent with glucose concentrations normalized to cell numbers and with mRNA sequencing data.

## 4.2 | Human forebrain spheroid EV cargo analysis by proteomics and miRNA sequencing

EVs from the three conditions and two seeding densities had a similar mean size of ~200 nm, indicating that the dynamic environment did not significantly affect EV size. MC condition showed the highest EV numbers per cell, 6-well condition showed the least, and Agg condition was in between. The pattern matched the expression of EV biogenesis genes Rab7a and STAM2 tested by RT-qPCR, but not much by transcriptome analysis. The transcriptome analysis showed similar EV biogenesis genes for Agg and MC groups, indicating that the higher EV yield of MC group may be due to the easy EV release into the medium compared to the Agg group which may contain more matrix-bound vesicles (Liu et al., 2023; Muok et al., 2024). VWBRs greatly improved EV generation of differentiated iPSCs, especially when cells were on microcarriers versus as aggregates. This observation is consistent with our previous study about undifferentiated iPSC-derived EVs in VWBRs, which showed the increased EV yield by MC group (Muok et al., 2024). In VWBRs, there are mainly three types of mechanical forces: shear, tension, and compression which influence EV release. Shear may directly sever EVs when ligand binding creates membrane tethers, tension on cells promotes exocytosis of EVs, and compression on cells enhances blebbing of EVs (Thompson & Papoutsakis, 2023). Besides, it was proposed that high intracellular levels of Ca<sup>2+</sup> are related to EV production in MSCs (Kang et al., 2022). In this study, Agg and MC exhibited lower Ca<sup>2+</sup> concentrations in the media, which indicated more Ca<sup>2+</sup> influx and, thus, higher EV generation.

The mechanical stresses on spheroids not only have an influence on EV quantities but may also affect EV qualities by regulating the cargo packaging process. In this study, EVs from the three conditions exhibited distinct distributions in PCA plot. Agg was above 6-well by 632 total proteins and MC was above 6-well by 513 total proteins. Clearly, Agg-EVs contained 119 more proteins than MC-EVs. However, in our previous study, there were 534 less proteins for the Agg-EV group than MC-EV group for undifferentiated iPSCs (Muok et al., 2024). This indicates that whether Agg or MC promotes protein packaging related to the cell type. PCA plots confirmed that differences in protein cargo of Agg versus 6-well (indicating the effect of hydrodynamic microenvironment) were larger than Agg versus MC (indicating the effect of 3D organization). EVs from the three culture conditions were enriched with different proteins. For example, 6-well EVs had more albumin (ALB), Agg was abundant in nerve growth factor inducible (VGF) and Filamin C (FLNC), and MC contained more fibroblast growth factor receptor 1 (FGFR1) and fatty acid synthase (FASN). As the DEPs in EV protein cargo showed some correlations with DEGs from transcriptome analysis, the EVs of Agg group may come from more diversified cell types with forebrain regional identity and the MC group may be more at the early forebrain development. For miRNA cargos, a subset of miRNAs in the parent cells were packaged into the EVs from Agg and MC. The top 15 abundant miRNAs were similar for Agg and MC groups, but expressed at a different abundant level.

The differentially expressed miRNAs (e.g., miR-126, 148b, 143, 92a, etc.) in the EVs of Agg and MC groups played distinct roles in regulating various pathways such as Wnt pathway, apoptosis, cell cycle, etc. (Muok et al., 2024; Yuan et al., 2022).

EVs recapitulate the beneficial effects of their parent cells because their cargo is selectively packaged from the parent cells through EV biogenesis pathways (Maumus et al., 2020). For example, cardiovascular progenitor-derived EVs triggered a reparative immune response in infarcted hearts; neutrophil-derived EVs could be anti- or pro-inflammatory depending on the triggering agents; astrocyte-derived EVs enhanced the survival and electrophysiological function of cortical neurons (Chun et al., 2021; Kolonics et al., 2020; Lima Correa et al., 2021). For forebrain spheroid-derived EVs, they are expected to show neuroprotective effects, and both our proteomics and miRNA-Seq analysis revealed axon guidance pathway. In a study of human brain tissue-derived EVs, the protein profile analysis revealed that the top 20 KEGG pathways were mainly related to synapse, metabolism and signaling pathways (Huang et al., 2020). In our study, even though the differentiated forebrain spheroids were at an early stage of brain tissue development, their EV proteins were identified to be involved in similar metabolism and signalling pathways to the brain tissue-derived EVs (Huang et al., 2020). Brain tissue-derived EVs were enriched in many miRNAs that were also abundant in these forebrain spheroid-derived EVs, such as miR-21-5p, miR-7-5p, miR-222-3p, etc. EVs from human iPSC-derived neural stem cells showed that their miRNAs were involved in many signaling and regulatory pathways of the central nervous system, which could be found either in proteomics data or miRNA-Seq data of our study, such as Hippo signaling pathway, glioma, prion disease, etc. (Upadhyaya et al., 2020).

### 4.3 | Function of biomanufactured human forebrain spheroid EVs

Human forebrain spheroid EVs were evaluated in an in vitro stroke model, which was D30 forebrain organoids underwent 3 h oxygen and glucose deprivation. MTT and Caspase 3/7 assays revealed that EVs from Agg, MC and 6-well conditions at low (300 particles/cell) and medium (1000 particles/cell) doses could enhance metabolic activities and reduce apoptosis, but the ROS did not change significantly. At the molecular level, glycolytic genes and pentose phosphate genes were up or down-regulated, but genes that related to NADH generation (Briere et al., 2006) were barely regulated. *Casp3* was reduced, and *CAT* was enhanced, which indicated decreased apoptosis and increased ROS scavenging ability. In terms of immune modulation, EVs tended to augment the anti-inflammatory response during recovery. Proteins and miRNAs from EVs that target the examined genes or pathways of functional analysis were identified (Tables S4 and S5). For protein cargo, the function-related proteins include apoptosis inhibitor or regulator API5, CCAR1 and CCAR2; ROS function protein CAT, and anti-inflammatory proteins ARG1, ILF2, ILF3, TGFBI and TNFRSF10B. The top significant pathway was TCA cycle, and the TCA cycle gene expression in the EV-treated iFCo was also altered in the in vitro OGD model. Several publications have mentioned that exosomes carrying metabolites reprogram recipient cell metabolism (Tan et al., 2023; Yang et al., 2020). The bioreactor EVs carry not only enzymes from TCA cycle, but also small metabolites which require future metabolism analysis. For miRNA cargo, the relevant miRNAs in regulating cell proliferation (e.g., miR-92a, 34a, 221, etc.), apoptosis (e.g., miR-30, 224, 146, etc.), ROS scavenging (e.g., miR-30, 7, 20, 17, 222, etc.), and anti-inflammation (e.g., miR-21, 7, 23a, 34a, 335, etc.) were identified, which may be attributed to the observed functional properties. By searching the miRTarBase, *TGFBI* is the miR-21-5p target gene, and *OGDH*, *CASP3*, *ARG1* and *TGFBI* are the target genes for miR-30a-5p. The function of miRNAs is not only directly downregulating gene expression but also regulating the whole pathway in coordination with other miRs and proteins. Therefore, the correlation between omics analysis and EV functional results was observed (Figure S16).

Currently, EVs used for brain diseases and injuries are mainly from MSCs (Lino et al., 2021), but there exists evidence that EVs from NPCs were comparable or better to MSC-EVs in enhancing neurological recovery and neuroregeneration of ischemia stroked mice (Zhang et al., 2019; Zheng et al., 2021). In another study, iPSC-derived neural stem cells were more efficient in improving lesion volume, motor function and episodic memory formation of thromboembolic stroked rodents than EVs from iPSC-derived MSCs (Webb et al., 2018). Neural stem/progenitor cell-secreted EVs also protected against Parkinson's disease pathologies, mitigated hallmarks of Alzheimer's disease, attenuated apoptosis and neuroinflammation after traumatic spinal cord injury, favoured neuronal differentiation and plasticity under stress conditions, counteracted the high-fat diet-dependent depletion of hippocampal neurogenic niche, etc. (Apodaca et al., 2021; Lee et al., 2022; Natale et al., 2022; Ocaña et al., 2023; Rong et al., 2019). However, the in vitro 2D neural stem/progenitor cell culture lacks interaction with other types of brain cells, such as neurons, astrocytes and microglia, and EVs from these types of cells modulate cell-to-cell communication, neurorepairment and neurodegeneration (Paolicelli et al., 2019; Peng et al., 2021; Upadhyaya et al., 2020). With a 3D dynamic culture environment such as VWBR, and a longer culture period (to allow spheroids to become organoids), cell diversity would increase. With a coculture system, that is, organoids plus mesoderm originated microglia and endothelial cells, the maturity of brain organoids would be promoted, thus generating more therapeutically potent EVs (Matsui et al., 2021; Song et al., 2019; Song et al., 2019; Zhang et al., 2023). The further scale-up of the VWBR should consider the oxygen and nutrients delivery and well-controlled physicochemical microenvironment. The biomanufactured EVs may be lyophilized for long-term storage as off-the-shelf products (Yuan et al., 2021).

## 5 | CONCLUSIONS

This study demonstrated that the aggregate and microcarrier-based differentiation of human forebrain spheroids in VWBRs generated significantly more EVs (up to 240–750 fold) than static aggregates. EV proteomics revealed that Agg condition shared more resemblance with MC than with 6-well condition. EV miRNA sequencing demonstrated that Agg and MC groups had similar types of miRNAs but at different abundant levels. Agg EV and MC EV showed therapeutic effects on in vitro OGD stroke model. Our results reveal a systematic and comprehensive analysis of proteome and miRNA profiles of EVs secreted by human forebrain spheroids in a dynamic VWBR. This study provides a scalable biomanufacturing platform with defined cargo profiles for human forebrain spheroid EV production for applications in drug delivery and cell-free therapy in pre-clinical settings.

### AUTHOR CONTRIBUTIONS

**Chang Liu:** Conceptualization; data curation; formal analysis; investigation; methodology; visualization; writing—original draft. **Li Sun:** Data curation; formal analysis; investigation; methodology; software; writing—review and editing. **Hannah Worden:** Data curation; investigation; methodology. **Justice Ene:** Data curation; investigation; methodology. **Olivia Zeng:** Data curation; investigation; methodology. **Jamini Bhagu:** Investigation; methodology. **Samuel C. Grant:** Investigation; Methodology; Supervision. **Xiaoping Bao:** Data curation; investigation; methodology. **Sunghoon Jung:** Conceptualization; investigation; methodology; project administration; resources. **Yan Li:** Conceptualization; data curation; formal analysis; funding acquisition; investigation; methodology; project administration; resources; supervision; writing—original draft; writing—review and editing.

### ACKNOWLEDGEMENTS

The authors would thank for the support by FSU Flow Cytometry core facility and FSU College of Medicine Translational Science Laboratory (Dr. Cynthia Vied) for proteomics, mRNA-seq and miRNA-seq, Dr. Brian K. Washburn at FSU Department of Biological Sciences for his help with RT-qPCR analysis. The authors also appreciate Dr. Breanna Borys at PBS Biotech Inc. for the help with experimental design. This work is supported by the National Science Foundation CAREER Award (CBET-1652992 and CBET-1917618). The Hitachi HT7800 for TEM was funded from NSF grant 2017869. A portion of this work was performed at the National High Magnetic Field Laboratory, which is supported by National Science Foundation Cooperative Agreement No. DMR-2128556 and the State of Florida. Research reported in this publication was also partially supported by the National Institutes of Health (USA) under Award No. R01NS125016 (to Y.L.) and R01NS102395 (to S.C.G.). The content is solely the responsibility of the authors and does not necessarily represent the official views of the National Institutes of Health.

### CONFLICT OF INTEREST STATEMENT

The authors declare no conflicts of interest.

### DATA AVAILABILITY STATEMENT

The datasets generated during and/or analyzed during the current study are available from the corresponding authors on reasonable request.

### ORCID

Chang Liu  <https://orcid.org/0000-0002-2749-7542>

Li Sun  <https://orcid.org/0000-0001-8228-7487>

Justice Ene  <https://orcid.org/0009-0004-4723-7299>

Samuel C. Grant  <https://orcid.org/0000-0001-7738-168X>

Yan Li  <https://orcid.org/0000-0002-5938-8519>

### REFERENCES

- Abdollahi, S. (2021). Extracellular vesicles from organoids and 3D culture systems. *Biotechnology and Bioengineering*, 118(3), 1029–1049.
- Apodaca, L. A., Baddour, A. A. D., Garcia, C., Alikhani, L., Giedzinski, E., Ru, N., Agrawal, A., Acharya, M. M., & Baulch, J. E. (2021). Human neural stem cell-derived extracellular vesicles mitigate hallmarks of Alzheimer's disease. *Alzheimer's Research & Therapy*, 13(1), 1–18.
- Arthur, P., Kandoi, K., Sun, L., Kalvala, A., Kuthleria, S., Bhattacharaya, S., Kulkarni, T., Nimma, R., Li, Y., Lamba, D. A., & Sing, M. (2023). Biophysical, molecular and proteomic profiling of human retinal organoids derived exosomes. *Pharmacological Research*, 40(4), 801–816.
- Benito-Kwiecinski, S., & Lancaster, M. A. (2020). Brain organoids: Human neurodevelopment in a dish. *Cold Spring Harbor Perspectives in Biology*, 12(8), a035709.
- Borys, B. S., Dang, T., So, T., Rohani, L., Revay, T., Walsh, T., Thompson, M., Argiropoulos, B., Rancourt, D. E., & Jung, S. (2021). Overcoming bioprocess bottlenecks in the large-scale expansion of high-quality hiPSC aggregates in vertical-wheel stirred suspension bioreactors. *Stem Cell Research & Therapy*, 12(1), 1–19.
- Borys, B. S., So, T., Colter, J., Dang, T., Roberts, E. L., Revay, T., Larijani, L., Krawetz, R., Lewis, I., & Argiropoulos, B. (2020). Optimized serial expansion of human induced pluripotent stem cells using low-density inoculation to generate clinically relevant quantities in vertical-wheel bioreactors. *Stem Cells Translational Medicine*, 9(9), 1036–1052.
- Briere, J.-J., Favier, J., Gimenez-Roqueplo, A.-P., & Rustin, P. (2006). Tricarboxylic acid cycle dysfunction as a cause of human diseases and tumor formation. *American Journal of Physiology-Cell Physiology*, 291(6), C1114–C1120.



- Buzas, E. I. (2023). The roles of extracellular vesicles in the immune system. *Nature Reviews Immunology*, 23(4), 236–250.
- Chen, X., Liu, C., Wadsworth, M., Zeng, E. Z., Driscoll, T., Zeng, C., & Li, Y. (2023). Surface engineering of auxetic scaffolds for neural and vascular differentiation from human pluripotent stem cells. *Advanced Healthcare Materials*, 12(6), 2202511.
- Cheng, L., & Hill, A. F. (2022). Therapeutically harnessing extracellular vesicles. *Nature Reviews Drug Discovery*, 21(5), 379–399.
- Chiaradia, I., & Lancaster, M. A. (2020). Brain organoids for the study of human neurobiology at the interface of in vitro and in vivo. *Nature Neuroscience*, 23(12), 1496–1508.
- Choi, N. Y., Lee, M.-Y., & Jeong, S. (2022). Recent advances in 3D-cultured brain tissue models derived from human iPSCs. *BioChip Journal*, 16(3), 246–254.
- Chun, C., Smith, A. S., Kim, H., Kamenz, D. S., Lee, J. H., Lee, J. B., Mack, D. L., Bothwell, M., Clelland, C. D., & Kim, D.-H. (2021). Astrocyte-derived extracellular vesicles enhance the survival and electrophysiological function of human cortical neurons in vitro. *Biomaterials*, 271, 120700.
- Dadheech, N., Bermudez de Leon, M., Cuesta-Gomez, N., Jasra, I. T., Pawlick, R., Marfil-Garza, B., Verhoeff, K., Sapkota, S., Razavy, H., & Anwar, P. (2023). Complete suspension differentiation of human pluripotent stem cells into pancreatic islets using vertical-wheel bioreactors. *Biorxiv*, 2023.08.09.552676.
- Dang, T., Borys, B. S., Kanwar, S., Colter, J., Worden, H., Blatchford, A., Croughan, M. S., Hossan, T., Rancourt, D. E., & Lee, B. (2021). Computational fluid dynamic characterization of vertical-wheel bioreactors used for effective scale-up of human induced pluripotent stem cell aggregate culture. *The Canadian Journal of Chemical Engineering*, 99(11), 2536–2553.
- de Almeida Fuzeta, M., Bernardes, N., Oliveira, F. D., Costa, A. C., Fernandes-Platzgummer, A., Farinha, J. P., Rodrigues, C. A., Jung, S., Tseng, R.-J., & Milligan, W. (2020). Scalable production of human mesenchymal stromal cell-derived extracellular vesicles under serum-/xeno-free conditions in a microcarrier-based bioreactor culture system. *Frontiers in Cell and Developmental Biology*, 8, 553444.
- de Sousa Pinto, D., Bandejas, C., de Almeida Fuzeta, M., Rodrigues, C. A., Jung, S., Hashimura, Y., Tseng, R. J., Milligan, W., Lee, B., & Ferreira, F. C. (2019). Scalable manufacturing of human mesenchymal stromal cells in the vertical-wheel bioreactor system: An experimental and economic approach. *Biotechnology Journal*, 14(8), 1800716.
- Di Lullo, E., & Kriegstein, A. R. (2017). The use of brain organoids to investigate neural development and disease. *Nature Reviews Neuroscience*, 18(10), 573–584.
- Gudbergsson, J. M., Johnsen, K. B., Skov, M. N., & Duroux, M. (2016). Systematic review of factors influencing extracellular vesicle yield from cell cultures. *Cytotechnology*, 68, 579–592.
- Gupta, D., Zickler, A. M., & El Andaloussi, S. (2021). Dosing extracellular vesicles. *Advanced Drug Delivery Reviews*, 178, 113961.
- Horiguchi, I., & Kino-oka, M. (2021). Current developments in the stable production of human induced pluripotent stem cells. *Engineering*, 7(2), 144–152.
- Huang, X., Huang, Z., Gao, W., Gao, W., He, R., Li, Y., Crawford, R., Zhou, Y., Xiao, L., & Xiao, Y. (2022). Current advances in 3D dynamic cell culture systems. *Gels*, 8(12), 829.
- Huang, Y., Cheng, L., Turchinovich, A., Mahairaki, V., Troncoso, J. C., Pletniková, O., Haughey, N. J., Vella, L. J., Hill, A. F., & Zheng, L. (2020). Influence of species and processing parameters on recovery and content of brain tissue-derived extracellular vesicles. *Journal of Extracellular Vesicles*, 9(1), 1785746.
- Hurwitz, S. N., & Meckes, D. G., Jr. (2017). An adaptable polyethylene glycol-based workflow for proteomic analysis of extracellular vesicles. *Methods in Molecular Biology*, 1660, 303–317.
- Hurwitz, S. N., Sun, L., Cole, K. Y., Ford, C. R., 3rd, Olcese, J. M., & Meckes, D. G., Jr. (2018). An optimized method for enrichment of whole brain-derived extracellular vesicles reveals insight into neurodegenerative processes in a mouse model of Alzheimer's disease. *Journal of Neuroscience Methods*, 307, 210–220.
- Jalilian, E., Massoumi, H., Bigit, B., Amin, S., Katz, E. A., Guaiquil, V. H., Anwar, K. N., Hematti, P., Rosenblatt, M. I., & Djililian, A. R. (2022). Bone marrow mesenchymal stromal cells in a 3D system produce higher concentration of extracellular vesicles (EVs) with increased complexity and enhanced neuronal growth properties. *Stem Cell Research & Therapy*, 13(1), 425.
- Jeske, R., Liu, C., Duke, L., Castro, M. L. C., Muok, L., Arthur, P., Singh, M., Jung, S., Sun, L., & Li, Y. (2023). Upscaling human mesenchymal stromal cell production in a novel vertical-wheel bioreactor enhances extracellular vesicle secretion and cargo profile. *Bioactive Materials*, 25, 732–747.
- Jones, M. C., Zha, J., & Humphries, M. J. (2019). Connections between the cell cycle, cell adhesion and the cytoskeleton. *Philosophical Transactions of the Royal Society B*, 374(1779), 20180227.
- Kang, H., Bae, Y. H., Kwon, Y., Kim, S., & Park, J. (2022). Extracellular vesicles generated using bioreactors and their therapeutic effect on the acute kidney injury model. *Advanced Healthcare Materials*, 11(4), 2101606.
- Khamis, Z. I., Sarker, D. B., Xue, Y., Al-Akkary, N., James, V. D., Zeng, C., Li, Y., & Sang, Q. X. (2023). Modeling human brain tumors and the microenvironment using induced pluripotent stem cells. *Cancers*, 15, 1253.
- Ko, E., Poon, M. L. S., Park, E., Cho, Y., & Shin, J. H. (2021). Engineering 3D cortical spheroids for an in vitro ischemic stroke model. *ACS Biomaterials Science & Engineering*, 7(8), 3845–3860.
- Kolonics, F., Szeifert, V., Timár, C. I., Ligeti, E., & Lőrincz, Á. M. (2020). The functional heterogeneity of neutrophil-derived extracellular vesicles reflects the status of the parent cell. *Cells*, 9(12), 2718.
- Kumar, A., & Starly, B. (2015). Large scale industrialized cell expansion: Producing the critical raw material for biofabrication processes. *Biofabrication*, 7(4), 044103.
- Lee, E. J., Choi, Y., Lee, H. J., Hwang, D. W., & Lee, D. S. (2022). Human neural stem cell-derived extracellular vesicles protect against Parkinson's disease pathologies. *Journal of Nanobiotechnology*, 20(1), 1–20.
- Lembong, J., Kirian, R., Takacs, J. D., Olsen, T. R., Lock, L. T., Rowley, J. A., & Ahsan, T. (2020). Bioreactor parameters for microcarrier-based human MSC expansion under xeno-free conditions in a vertical-wheel system. *Bioengineering*, 7(3), 73.
- Lima Correa, B., El Harane, N., Gomez, I., Rachid Hocine, H., Vilar, J., Desgres, M., Bellamy, V., Keirthisana, K., Guillas, C., & Perotto, M. (2021). Extracellular vesicles from human cardiovascular progenitors trigger a reparative immune response in infarcted hearts. *Cardiovascular Research*, 117(1), 292–307.
- Lino, M. M., Simoes, S., Tomatis, F., Albino, I., Barrera, A., Vivien, D., Sobrino, T., & Ferreira, L. (2021). Engineered extracellular vesicles as brain therapeutics. *Journal of Controlled Release*, 338, 472–485.
- Liu, C., Chen, X., Liu, Y., Sun, L., Yu, Z., Ren, Y., Zeng, C., & Li, Y. (2023). Engineering extracellular matrix-bound nanovesicles secreted by three-dimensional human mesenchymal stem cells. *Advanced Healthcare Materials*, 12(27), e2301112.
- Liu, C., Helsper, S., Marzano, M., Chen, X., Muok, L., Esmonde, C., Zeng, C., Sun, L., Grant, S. C., & Li, Y. (2022). Human forebrain organoid-derived extracellular vesicle labeling with iron oxides for in vitro magnetic resonance imaging. *Biomedicine*, 10(12), 3060.
- Liu, D., Chen, S., & Win Naing, M. (2021). A review of manufacturing capabilities of cell spheroid generation technologies and future development. *Biotechnology and Bioengineering*, 118(2), 542–554.
- Marzano, M., Bejoy, J., Cheerathodi, M., Sun, L., York, S., Zhao, J., Kanekiyo, T., Bu, G., Meckes, D. G., Jr., & Li, Y. (2019). Differential effects of extracellular vesicles of lineage-specific human pluripotent stem cells on cellular behaviours of isogenic cortical spheroids. *Cells*, 8, 993–1014.
- Marzano, M., Bou-Dargham, M. J., Cone, A. S., York, S., Helsper, S., Grant, S. C., Meckes, D. G., Jr., Sang, Q. X., & Li, Y. (2021). Biogenesis of extracellular vesicles produced from human stem cell-derived cortical spheroids exposed to iron oxides. *ACS Biomaterials Science & Engineering*, 7(3), 1111–1122.

- Matsui, T. K., Tsuru, Y., Hasegawa, K., & Kuwako, K. I. (2021). Vascularization of human brain organoids. *Stem Cells*, 39(8), 1017–1024.
- Maumus, M., Rozier, P., Boulestreau, J., Jorgensen, C., & Noël, D. (2020). Mesenchymal stem cell-derived extracellular vesicles: Opportunities and challenges for clinical translation. *Frontiers in Bioengineering and Biotechnology*, 8, 997.
- Muok, L., Sun, L., Esmonde, C., Worden, H., Vied, C., Duke, L., Ma, S., Zeng, O. Z., Driscoll, T. P., Jung, S., & Li, Y. (2024). Extracellular vesicle biogenesis of three-dimensional human pluripotent stem cells in a novel vertical-wheel bioreactor. *Journal of Extracellular Biology*, 3, e133.
- Murphy, K. C., Fang, S. Y., & Leach, J. K. (2014). Human mesenchymal stem cell spheroids in fibrin hydrogels exhibit improved cell survival and potential for bone healing. *Cell and Tissue Research*, 357, 91–99.
- Murphy, K. C., Hung, B. P., Browne-Bourne, S., Zhou, D., Yeung, J., Genetos, D. C., & Leach, J. K. (2017). Measurement of oxygen tension within mesenchymal stem cell spheroids. *Journal of The Royal Society Interface*, 14(127), 20160851.
- Natale, F., Leone, L., Rinaudo, M., Sollazzo, R., Barbati, S. A., Greca, F. La, Spinelli, M., Fusco, S., & Grassi, C. (2022). Neural stem cell-derived extracellular vesicles counteract insulin resistance-induced senescence of neurogenic niche. *Stem Cells*, 40(3), 318–331.
- Nathani, A., Sun, L., Khan, I., Aare, M., Bagde, A., Li, Y., & Singh, M. (2024). Combined role of interleukin-15 stimulated natural killer cell-derived extracellular vesicles and carboplatin in Osimertinib resistant H1975 lung cancer cells with EGFR mutation. *Pharmaceutics*, 16, 83.
- Nogueira, D. E., Rodrigues, C. A., Carvalho, M. S., Miranda, C. C., Hashimura, Y., Jung, S., Lee, B., & Cabral, J. M. (2019). Strategies for the expansion of human induced pluripotent stem cells as aggregates in single-use Vertical-Wheel™ bioreactors. *Journal of Biological Engineering*, 13, 1–14.
- Ocaña, S. D., Magaquian, D., & Banchio, C. (2023). Neural stem cell-derived extracellular vesicles favour neuronal differentiation and plasticity under stress conditions. *Frontiers in Molecular Neuroscience*, 16, 1146592.
- Otahal, A., Kramer, K., Moser, L., Lacza, Z., Nehrer, S., & De Luna, A. (2023). Priming of Hoffa-derived MSC with IL1B in vertical wheel bioreactor culture yields extracellular vesicles hindering chondrocyte recovery compared to unstimulated MSCs. *Osteoarthritis and Cartilage*, 31, S28.
- Paolicelli, R. C., Bergamini, G., & Rajendran, L. (2019). Cell-to-cell communication by extracellular vesicles: Focus on microglia. *Neuroscience*, 405, 148–157.
- Park, D. S., Kozaki, T., Tiwari, S. K., Moreira, M., Khalilnezhad, A., Torta, F., Olivie, N., Thiam, C. H., Liani, O., Silvini, A., Phoo, W. W., Gao, L., Triebel, A., Tham, W. K., Goncalves, L., Kong, W. T., Raman, S., Zhang, X. M., Dunsmore, G., ... Ginhoux, F. (2023). iPS-cell-derived microglia promote brain organoid maturation via cholesterol transfer. *Nature*, 623, 397–405.
- Pasca, S. P. (2018). The rise of three-dimensional human brain cultures. *Nature*, 553(7689), 437–445.
- Pauwels, M. J., Xie, J., Ceroi, A., Balusu, S., Castelein, J., Van Wouterghem, E., Van Imschoot, G., Ward, A., Menhenniott, T. R., & Gustafsson, O. (2022). Choroid plexus-derived extracellular vesicles exhibit brain targeting characteristics. *Biomaterials*, 290, 121830.
- Peng, H., Harvey, B. T., Richards, C. I., & Nixon, K. (2021). Neuron-derived extracellular vesicles modulate microglia activation and function. *Biology*, 10(10), 948.
- Penney, J., Ralvenius, W. T., & Tsai, L.-H. (2020). Modeling Alzheimer's disease with iPSC-derived brain cells. *Molecular Psychiatry*, 25(1), 148–167.
- Qian, X., Nguyen, H. N., Song, M. M., Hadiono, C., Ogden, S. C., Hammack, C., Yao, B., Hamersky, G. R., Jacob, F., & Zhong, C. (2016). Brain-region-specific organoids using mini-bioreactors for modeling ZIKV exposure. *Cell*, 165(5), 1238–1254.
- Raposo, G., & Stahl, P. D. (2019). Extracellular vesicles: A new communication paradigm? *Nature Reviews Molecular Cell Biology*, 20(9), 509–510.
- Ray, R. P., Matamoros-Vidal, A., Ribeiro, P. S., Tapon, N., Houle, D., & Thompson, B. J. (2015). Patterned anchorage to the apical extracellular matrix defines tissue shape in the developing appendages of *Drosophila*. *Developmental Cell*, 34(3), 310–322.
- Rider, M. A., Hurwitz, S. N., & Meckes, D. G., Jr. (2016). ExtraPEG: A polyethylene glycol-based method for enrichment of extracellular vesicles. *Scientific Reports*, 6, 23978.
- Rodrigues, C. A., Silva, T. P., Nogueira, D. E., Fernandes, T. G., Hashimura, Y., Wesselschmidt, R., Diogo, M. M., Lee, B., & Cabral, J. M. (2018). Scalable culture of human induced pluripotent cells on microcarriers under xeno-free conditions using single-use vertical-wheel™ bioreactors. *Journal of Chemical Technology & Biotechnology*, 93(12), 3597–3606.
- Rong, Y., Liu, W., Wang, J., Fan, J., Luo, Y., Li, L., Kong, F., Chen, J., Tang, P., & Cai, W. (2019). Neural stem cell-derived small extracellular vesicles attenuate apoptosis and neuroinflammation after traumatic spinal cord injury by activating autophagy. *Cell Death & Disease*, 10(5), 340.
- Silva, T. P., Sousa-Luís, R., Fernandes, T. G., Bekman, E. P., Rodrigues, C. A., Vaz, S. H., Moreira, L. M., Hashimura, Y., Jung, S., & Lee, B. (2021). Transcriptome profiling of human pluripotent stem cell-derived cerebellar organoids reveals faster commitment under dynamic conditions. *Biotechnology and Bioengineering*, 118(7), 2781–2803.
- Song, L., Wang, K., Li, Y., & Yang, Y. (2016). Nanotopography promoted neuronal differentiation of human induced pluripotent stem cells. *Colloids and Surfaces B: Biointerfaces*, 148, 49–58.
- Song, L., Yuan, X., Jones, Z., Griffin, K., Zhou, Y., Ma, T., & Li, Y. (2019). Assembly of human stem cell-derived cortical spheroids and vascular spheroids to model 3-D brain-like tissues. *Scientific Reports*, 9(1), 5977.
- Song, L., Yuan, X., Jones, Z., Vied, C., Miao, Y., Marzano, M., Hua, T., Sang, Q.-X. A., Guan, J., & Ma, T. (2019). Functionalization of brain region-specific spheroids with isogenic microglia-like cells. *Scientific Reports*, 9(1), 11055.
- Sousa, M. F., Silva, M. M., Giroux, D., Hashimura, Y., Wesselschmidt, R., Lee, B., Roldão, A., Carrondo, M. J., Alves, P. M., & Serra, M. (2015). Production of oncolytic adenovirus and human mesenchymal stem cells in a single-use, vertical-wheel bioreactor system: Impact of bioreactor design on performance of microcarrier-based cell culture processes. *Biotechnology Progress*, 31(6), 1600–1612.
- Tan, H. Y., Cho, H., & Lee, L. P. (2021). Human mini-brain models. *Nature Biomedical Engineering*, 5(1), 11–25.
- Tan, S., Yang, Y., Yang, W., Han, Y., Huang, L., Yang, R., Hu, Z., Tao, Y., Liu, L., Li, Y., Oyang, L., Lin, J., Peng, Q., Jiang, X., Xu, X., Xia, L., Peng, M., Wu, N., Tang, Y., ... Zhou, Y. (2023). Exosomal cargos-mediated metabolic reprogramming in tumor microenvironment. *Journal of Experimental & Clinical Cancer Research*, 42(1), 59.
- Teryek, M., Jadhav, P., Bento, R., & Parekkadan, B. (2023). High-throughput production of microcapsules for human bone marrow derived mesenchymal stem cell biomanufacturing in a vertical-wheel bioreactor. *Biotechnology and Bioprocess Engineering*, 28(4), 528–544.
- Thompson, W., & Papoutsakis, E. T. (2023). The role of biomechanical stress in extracellular vesicle formation, composition and activity. *Biotechnology Advances*, 66, 108158.
- Tian, T., Cao, L., He, C., Ye, Q., Liang, R., You, W., Zhang, H., Wu, J., Ye, J., & Tannous, B. A. (2021). Targeted delivery of neural progenitor cell-derived extracellular vesicles for anti-inflammation after cerebral ischemia. *Theranostics*, 11(13), 6507.
- Upadhy, R., Madhu, L. N., Attaluri, S., Gitai, D. L. G., Pinson, M. R., Kodali, M., Shetty, G., Zanirati, G., Kumar, S., & Shuai, B. (2020). Extracellular vesicles from human iPSC-derived neural stem cells: MiRNA and protein signatures, and anti-inflammatory and neurogenic properties. *Journal of Extracellular Vesicles*, 9(1), 1809064.
- Upadhy, R., Zingg, W., Shetty, S., & Shetty, A. K. (2020). Astrocyte-derived extracellular vesicles: Neuroreparative properties and role in the pathogenesis of neurodegenerative disorders. *Journal of Controlled Release*, 323, 225–239.

- Vallabhaneni, H., Shah, T., Shah, P., & Hursh, D. A. (2023). Suspension culture on microcarriers and as aggregates enables expansion and differentiation of pluripotent stem cells (PSCs). *Cytotherapy*, 25(9), 993–1005.
- van Niel, G., Carter, D. R., Clayton, A., Lambert, D. W., Raposo, G., & Vader, P. (2022). Challenges and directions in studying cell–cell communication by extracellular vesicles. *Nature Reviews Molecular Cell Biology*, 23(5), 369–382.
- van Niel, G., D'Angelo, G., & Raposo, G. (2018). Shedding light on the cell biology of extracellular vesicles. *Nature Reviews Molecular Cell Biology*, 19(4), 213–228.
- Webb, R. L., Kaiser, E. E., Scoville, S. L., Thompson, T. A., Fatima, S., Pandya, C., Sriram, K., Swetenburg, R. L., Vaibhav, K., & Arbab, A. S. (2018). Human neural stem cell extracellular vesicles improve tissue and functional recovery in the murine thromboembolic stroke model. *Translational Stroke Research*, 9, 530–539.
- Welsh, J. A., Goberdhan, D. C. I., O'Driscoll, L., Buzas, E. I., Blenkiron, C., Bussolati, B., Cai, H., Di Vizio, D., Driedonks, T. A. P., Erdbrügger, U., Falcon-Perez, J. M., Fu, Q. L., Hill, A. F., Lenassi, M., Lim, S. K., Mahoney, M. G., Mohanty, S., Möller, A., Nieuwland, R., ... Witwer, K. W. (2024). Minimal information for studies of extracellular vesicles (MISEV2023): From basic to advanced approaches. *Journal of Extracellular Vesicles*, 13(2), e12404.
- Yang, E., Wang, X., Gong, Z., Yu, M., Wu, H., & Zhang, D. (2020). Exosome-mediated metabolic reprogramming: The emerging role in tumor microenvironment remodeling and its influence on cancer progression. *Signal Transduction and Targeted Therapy*, 5(1), 242.
- Yuan, F., Li, Y. M., & Wang, Z. (2021). Preserving extracellular vesicles for biomedical applications: Consideration of storage stability before and after isolation. *Drug Delivery*, 28(1), 1501–1509.
- Yuan, X., Chen, X., Zeng, C., Meckes, D. G., Jr., & Li, Y. (2022). Extracellular vesicle collection from human stem cells grown in suspension bioreactors. *Methods in Molecular Biology*, 2436, 193–204.
- Yuan, X., Sun, L., Jeske, R., Nkosi, D., York, S., Liu, Y., Grant, S. C., Meckes, D. G. J., & Li, Y. (2022). Engineering Extracellular Vesicles by Three-dimensional Dynamic Culture of Human Mesenchymal Stem Cells. *Journal of Extracellular Vesicles*, 11(6), e12235.
- Zhang, W., Jiang, J., Xu, Z., Yan, H., Tang, B., Liu, C., Chen, C., & Meng, Q. (2023). Microglia-containing human brain organoids for the study of brain development and pathology. *Molecular Psychiatry*, 28(1), 96–107.
- Zhang, Z., O'Laughlin, R., Song, H., & Ming, G. L. (2022). Patterning of brain organoids derived from human pluripotent stem cells. *Current Opinion in Neurobiology*, 74, 102536.
- Zhang, Z. G., Buller, B., & Chopp, M. (2019). Exosomes—beyond stem cells for restorative therapy in stroke and neurological injury. *Nature Reviews Neurology*, 15(4), 193–203.
- Zheng, X., Zhang, L., Kuang, Y., Venkataramani, V., Jin, F., Hein, K., Zafeiriou, M. P., Lenz, C., Moebius, W., & Kilic, E. (2021). Extracellular vesicles derived from neural progenitor cells—a preclinical evaluation for stroke treatment in mice. *Translational Stroke Research*, 12, 185–203.

## SUPPORTING INFORMATION

Additional supporting information can be found online in the Supporting Information section at the end of this article.

**How to cite this article:** Liu, C., Sun, L., Worden, H., Ene, J., Zeng, O. Z., Bhagu, J., Grant, S. C., Bao, X., Jung, S., & Li, Y. (2024). Profiling biomanufactured extracellular vesicles of human forebrain spheroids in a Vertical-Wheel Bioreactor. *Journal of Extracellular Biology*, 3, e70002. <https://doi.org/10.1002/jex2.70002>